Strongly coupled peridynamic and lattice Boltzmann models using immersed boundary method for flow-induced structural deformation and fracture

Ya Zhang[a], Sina Haeri[b], Guang Pan[c], Yonghao Zhang[b,*]

[a]*James Weir Fluids Laboratory, Department of Mechanical and Aerospace Engineering, University of Strathclyde, Glasgow, G1 1XJ, UK*
[b]*School of Engineering, The University of Edinburgh, Edinburgh, EH9 3EB, UK*
[c]*School of Marine Science and Technology, Northwestern Polytechnical University, Xi'an, 710072,China*

Abstract

To simulate the dynamics of structural deformation and fracture caused by fluid-structure interactions accurately and efficiently, a strong coupling between the peridynamic model and the lattice Boltzmann method using the immersed boundary method is developed here. In this novel method, the peridynamic model predicts structural deformation and fracture, the cascaded lattice Boltzmann method serves as the flow solver, and the immersed boundary method is to enforce a no-slip boundary condition on the fluid-solid interface. The strong coupling is achieved by adding velocity corrections for the fluid and solid phases simultaneously at each time step, which are calculated by solving a linear system of equations derived from an implicit velocity correction immersed boundary scheme. Therefore, this new scheme based on the immersed boundary method eliminates the need to iteratively solve the dynamics of the fluid and solid phases at each time step. The proposed method is rigorously validated considering the plate with a pre-existing crack under velocity boundary conditions, the sedimentation of an elastic disk, the cross-flow over a flexible beam, and the flow-induced deformation of an elastic beam attached to a rigid cylinder. More importantly, the structural deformation, crack formation, and

*Corresponding author
Email address: yonghao.zhang@ed.ac.uk (Yonghao Zhang)

fracture due to interaction with the fluid flow are captured innovatively.

Keywords: Peridynamics, immersed boundary method, lattice Boltzmann method, fluid-structure interaction, hydraulic fracturing, strong coupling
2010 MSC: 00-01, 99-00

1. Introduction

The formation and propagation of cracks and the breakup and movement of crack fragments in a fluid flow are of primary importance for many medical and industrial applications, such as rupture of the aneurysm [1], microstructural damage of articular cartilage [2], and silt erosion in hydro turbines [3]. Considering the great challenges in the development of analytical solutions and laboratory experiments for these complicated fluid-structure interaction (FSI) problems, an accurate and efficient numerical tool is key to developing novel FSI technologies and improving structure integrity of industrial systems.

As the continuity assumption underlying the classical continuum mechanics [4–6] becomes invalid in the presence of solid cracks, some researchers attempted to utilize other methods including the diffuse-interface model [7] and the particle-based model [8]. Here, we will use the peridynamics theory to describe structural deformation and dynamic fracture, which is implemented as a particle solver where the solid is discretized using a set of material points, and the interactions between these points are expressed in an integral form [9–11]. Hence, the continuity assumption is not required and the discontinuities such as fractures are captured inherently [12]. Moreover, many constitutive models have been developed for different materials, such as rubbery membranes [13], composite structures [14], brittle and ductile materials [15–17]. To build a consistent computational framework to model the dynamical processes of structural deformation, crack formation and propagation, and final breakup, the peridynamic theory as a solid solver is then coupled with a flow solver via a partitioned scheme for its flexibility [5, 6, 18, 19].

A coupled immersed boundary-cascaded lattice Boltzmann method (IB-CLBM) [20]

has been applied successfully for many complex FSI problems [18, 21–25]. The CLBM is a promising flow solver, which has been applied in the simulation of turbulent, multiphase [26], and thermal flows [27]. The immersed boundary method (IBM) [28] tracks the fluid-solid interface with a moving Lagrangian grid to effectively enforce the no-slip boundary condition on the interface [29–32], thereby circumventing the time-consuming re-meshing procedure used in conventional body conformal boundary schemes [33–38]. Moreover, it has been demonstrated that the relaxed multi-direct-forcing (MDF) scheme can significantly improve efficiency and accuracy of implementing the no-slip boundary condition in an IB scheme [22].

Coupling of the fluid and solid solvers using a partitioned approach can be achieved through a weak or strong scheme. We have previously developed a weak scheme to couple the peridynamic model with the IB-CLBM solver [39] by launching the two solvers sequentially. It has been demonstrated that this multi-physics computational framework can predict the erosive impact of solid particles in a flow correctly. Recently, a weak coupling scheme for the peridynamic model and an open-source solver based on the Navier-Stokes equations has also been achieved by Dalla Barba and Picano [40, 41]. However, in the above attempts, the solid-fluid density ratio should be much larger than unity and a sub-evolution step of the peridynamic solver is needed to ensure the numerical stability, as the numerical errors arise from the asynchronously satisfied interface condition in the weak coupling scheme [42].

Here, we will develop a strong coupling scheme, so the concurrent solutions of the fluid and solid phases will improve the temporal accuracy and numerical stability, which is essential to capturing structural deformation, crack formation and propagation, and breakup. The traditional strong coupling approach [29] is computationally expensive due to the iterative solution of fluid flow and structure dynamics until convergence at each time step. To alleviate this drawback, the IBM was used as an efficient bridge to connect the fluid and solid solvers within a linear system of equations. These efforts have been pioneered by Wang and Eldredge [43], Lācis et al. [44], Goza and Colonius [45], who demonstrated

that the iterative solution of the fluid and solid phases at each time step is not necessary.

Moreover, there are many iterative methods employed to solve the linear system of equations based on the IBM. For example, in the flow solvers based on the Navier-Stokes equations, the block-LU decomposition linear equation was employed to solve the implicit coupling between fluid dynamics and rigid body dynamics [44], and between fluid dynamics and thin elastic structures [45]. Wang and Eldredge [43] used a block Gauss-Seidel scheme to solve the strong coupling between the fluids and rigid-body systems, and a relaxation scheme based on the virtual fluid inertia was employed to reduce the number of iterations.

In the current paper, the peridynamic model and the LBM are coupled through a strong coupling scheme based on the IBM to model the flow-induced structural deformation and fracture. Different from using the force corrections like Wang and Eldredge [43], the velocity corrections for the fluid and solid phases are calculated by solving a linear system of equations derived from an implicit velocity correction scheme of the IBM. Moreover, the simultaneous velocity corrections in the current method are solved iteratively with the efficient relaxed MDF scheme of the IBM [22].

This paper is organised as follows. In Section 2, the peridynamic model and the IB-CLBM are introduced, the strong coupling scheme is derived, and the algorithm is summarised. In Section 3, the proposed method is validated rigorously by the plate with a pre-existing crack under velocity boundary conditions, the sedimentation of an elastic disk, the cross-flow over a deformable beam, and the flow-induced deformation of an elastic beam attached to a rigid cylinder. The conclusions are drawn in Section 4.

2. Methodology

2.1. The peridynamic theory

The peridynamic theory uses an integral equation to describe the relative displacement and force between neighbouring material points and hence it inherently captures the discontinuities, such as crack and material damages [46]. The peridynamic theory is introduced briefly here, and more information can be found in the literature, e.g. Refs. [11, 46]. Here, the variables of the peridynamic model are marked with a subscript s.

The peridynamic theory formulates the motion of material points as

$$\rho_s \ddot{\mathbf{d}}(\mathbf{x}_s, t) = \mathbf{F}_{pd}(\mathbf{x}_s, t) + \mathbf{F}_b(\mathbf{x}_s, t), \tag{1}$$

where ρ_s is the density of material points; $\mathbf{x}_s$ is the initial location of a material point, which refers to the material points moving in the Lagrangian frame; $\mathbf{d}$ is the displacement vector of the material point $\mathbf{x}_s$ at time t. The acceleration of each material particle $\ddot{\mathbf{d}}$ is related to the peridynamic long-range force term of the peridynamics $\mathbf{F}_{pd}$ and an external body force density $\mathbf{F}_b$. A bond-based peridynamic model is used to calculate $\mathbf{F}_{pd}$, i.e.

$$\mathbf{F}_{pd}(\mathbf{x}_s, t) = \sum_{\mathbf{x}'_s}^{H} \mathbf{f}(\eta, \xi) V_{\mathbf{x}'_s}. \tag{2}$$

In Eq. (2), H represents the neighbourhood of the material point $\mathbf{x}_s$, and the region is determined by a horizon radius $\delta = 3.015\Delta$, where Δ is the size of material points. Eq. (2) shows that the long-range force $\mathbf{F}_{pd}$, exerted on the material point $\mathbf{x}_s$ by the other points $\mathbf{x}'_s$ within H, is the integral of a force density $\mathbf{f}(\eta, \xi)$ over the volume $V_{\mathbf{x}'_s}$, where $\xi = \mathbf{x}'_s - \mathbf{x}_s$ and $\eta = \mathbf{d}' - \mathbf{d}$ [11].

A prototype micro-elastic brittle (PMB) material with a bond-based peridynamic formulation [46] is used in this study. The force density takes the form of

$$\mathbf{f}(\eta, \xi) = csk\mathbf{n}, \tag{3}$$

where the unit vector $\mathbf{n}$ points from $\mathbf{x}_s + \mathbf{d}$ to $\mathbf{x}'_s + \mathbf{d}'$. For two-dimensional structures, the bond constant c is defined as

$$c = 9E/\pi h\delta^3, \tag{4}$$

where E is the Young's modulus, and h is structure thickness ($h = \Delta$). The scalar bond stretch s in Eq. (3) is defined as

$$s = \frac{|\eta + \xi| - |\xi|}{|\xi|}. \tag{5}$$

If the bond stretch s exceeds a critical value s_c, the bond breaks irreversibly and k is set to be zero; otherwise, k is always kept to be one. The critical stretch s_c is obtained from

$$s_c = \sqrt{\frac{4G_c}{hc\delta^4}}, \tag{6}$$

where G_c is the fracture energy of the material. The accumulation of broken bonds leads to material damage. The damage of a material point is assessed with the ratio of the number of broken bonds to all the bonds of the material point, which equals one when a material point loses all its bonds [39].

The Störmer–Verlet integration with second-order accuracy is employed here to integrate Eq. (1) as follows,

$$\mathbf{d}_s^{n+1} = 2\mathbf{d}_s^n - \mathbf{d}_s^{n-1} + \delta t^2 \ddot{\mathbf{d}}_s^n, \tag{7}$$

$$\mathbf{u}_s^n = \dot{\mathbf{d}}_s^n = \frac{\mathbf{d}_s^{n+1} - \mathbf{d}_s^{n-1}}{2\delta t}. \tag{8}$$

2.2. The immersed boundary-cascaded lattice Boltzmann method

In the IB-CLBM method, the IBM is used to enforce the no-slip boundary condition on the fluid-solid interface, tracked with a moving Lagrangian grid $\mathbf{x}_l$, and the CLBM solves the fluid flow in the computational domain discretized with a fixed Eulerian mesh $\mathbf{x}$. The Lagrangian variables are marked with the subscript "l", while the Eulerian ones have no subscript.

In the CLBM, the fluid is represented by a set of imaginary particles that follow the collision-streaming procedures on a uniform lattice grid. The distribution of imaginary particles evolves according to the following equation,

$$f_\alpha(\mathbf{x}+\mathbf{e}_\alpha\delta t, t+\delta t) = f_\alpha(\mathbf{x},t) + \Omega_\alpha(\mathbf{x},t) + S_\alpha\delta t, \tag{9}$$

where f_α is the distribution function of imaginary particles at the position $\mathbf{x}$ with the discrete velocity $\mathbf{e}_\alpha$ at the time t; Ω_α, S_α and δt are the discrete collision operator, the discrete force term and the time step, respectively. The D2Q9 discrete velocity set $\mathbf{e} = |\mathbf{e}_\alpha\rangle'$ for two-dimensional flows [47] is

$$\mathbf{e} = \begin{bmatrix} 0 & 1 & 0 & -1 & 0 & 1 & -1 & -1 & 1 \\ 0 & 0 & 1 & 0 & -1 & 1 & 1 & -1 & -1 \end{bmatrix}, \tag{10}$$

where the superscript "$'$" is the transpose operator, $|\cdot\rangle$ represents a column vector. The relaxation parameters ω_α of the collision operator is calculated from the kinematic shear viscosity ν of the fluid as follows,

$$\nu = c_s^2(\omega_{4,5}^{-1} - 0.5), \tag{11}$$

$$\omega_4 = \omega_5, \tag{12}$$

where other relaxation parameters are set to unity, and c_s is the sound speed of the D2Q9 model, i.e. $c_s = 1/\sqrt{3}$. To minimize the compressibility effect in the LBM, the Mach number $Ma = u/c_s$ is chosen to be smaller than 0.1, which means the fluid velocity in lattice unit is always lower than 0.05.

The external force term $\mathbf{F}$ is incorporated in the central-moment collision operator $\mathbf{\Omega} = |\Omega_\alpha\rangle$, which is also related to the distribution functions $\mathbf{f} = |f_\alpha\rangle$ [48]. The discrete forcing term $\mathbf{S} = |S_\alpha\rangle$ is obtained from the external body force $\mathbf{F}$ [48]. The forcing scheme of the CLBM proposed by Premnath and Banerjee [48] takes the body force term into account through two steps, i.e. the collision operation and the velocity refinement. The macroscopic density ρ and

unrefined velocity $\mathbf{u}^*$ are calculated as

$$\rho(\mathbf{x},t) = \sum_{\alpha=0}^{8} f_\alpha(\mathbf{x},t), \tag{13}$$

$$\rho(\mathbf{x},t)\mathbf{u}^*(\mathbf{x},t) = \sum_{\alpha=0}^{8} \mathbf{e}_\alpha f_\alpha(\mathbf{x},t). \tag{14}$$

The velocity $\mathbf{u}^*$ is then refined with the velocity correction $\delta\mathbf{u}(\mathbf{x},t)$ as

$$\mathbf{u}(\mathbf{x},t) = \mathbf{u}^*(\mathbf{x},t) + \delta\mathbf{u}(\mathbf{x},t), \tag{15}$$

where $\delta\mathbf{u}(\mathbf{x},t) = \mathbf{F}\delta t/2\rho$.

If a no-slip boundary is fulfilled, the fluid velocity $\mathbf{u}$ at the location of Lagrangian points $\mathbf{x}_l$ should be the same as the solid velocity $\mathbf{u}_l$,

$$\mathbf{u}(\mathbf{x}_l,t) = \mathbf{u}_l(\mathbf{x}_l,t). \tag{16}$$

The fluid velocity at the Lagrangian points $\mathbf{x}_l$ is interpolated from the surrounding lattices using

$$\mathbf{u}(\mathbf{x}_l,t) = \sum_{\mathbf{x}} \mathbf{u}(\mathbf{x},t)\Phi(\mathbf{x}-\mathbf{x}_l)\delta x^2, \tag{17}$$

where δx is the lattice spacing. The 4-point regularised delta function Φ [33] is

$$\Phi(x,y) = \frac{1}{\delta x^2}\phi(\frac{x}{\delta x})\phi(\frac{y}{\delta x}), \tag{18}$$

and

$$\phi(r) = \begin{cases} \frac{1}{8}(3-2|r|+\sqrt{1+4|r|-4r^2}), & |r| \le 1 \\ \frac{1}{8}(5-2|r|-\sqrt{-7+12|r|-4r^2}), & 1 < |r| \le 2 \\ 0, & \text{otherwise.} \end{cases} \tag{19}$$

In order to achieve the no-slip boundary in Eq. (16), according to the implicit velocity correction scheme of the IBM [49], a velocity correction $\delta\mathbf{u}_l$ is applied to each Lagrangian point $\mathbf{x}_l$ and distributed onto the background Eulerian grid to obtain the velocity correction $\delta\mathbf{u}(\mathbf{x})$,

$$\delta\mathbf{u}(\mathbf{x},t) = \sum_{\mathbf{x}_l} \delta\mathbf{u}_l(\mathbf{x}_l,t)\Phi(\mathbf{x}-\mathbf{x}_l)\delta s_l, \tag{20}$$

where δs_l is the elemental surface of Lagrangian point l in two-dimensional simulations. The surface force density on the Lagrangian point $\mathbf{F}_l^{ib}(\mathbf{x}_l)$ can be obtained from

$$\mathbf{F}_l^{ib}(\mathbf{x}_l, t) = \frac{2\rho\delta\mathbf{u}_l(\mathbf{x}_l, t)}{\delta t}. \tag{21}$$

When the no-slip boundary condition in Eq. (16) is satisfied, the velocity $\mathbf{u}_l(\mathbf{x}_l)$ should satisfy the following equation [49],

$$\mathbf{u}_l(\mathbf{x}_l, t) = \sum_{\mathbf{x}} \left[\mathbf{u}^*(\mathbf{x}, t) + \sum_{\mathbf{x}_m} \delta\mathbf{u}_m(\mathbf{x}_m, t)\Phi(\mathbf{x} - \mathbf{x}_m)\delta s_m \right] \Phi(\mathbf{x} - \mathbf{x}_l)\delta x^2, \tag{22}$$

where both l and m represent the Lagrangian points. Considering all the Lagrangian points, Eq. (22) can be expressed as a system of linear equations [49],

$$\mathbf{A}\mathbf{y} = \mathbf{b}, \tag{23}$$

$$\mathbf{A}_{lm} = \sum_{\mathbf{x}} \Phi(\mathbf{x} - \mathbf{x}_m)\Phi(\mathbf{x} - \mathbf{x}_l)\delta s_m \delta x^2, \tag{24}$$

$$\mathbf{y}_m = \delta\mathbf{u}_m(\mathbf{x}_m), \tag{25}$$

$$\mathbf{b}_l = \mathbf{u}_l(\mathbf{x}_l) - \sum_{\mathbf{x}} \mathbf{u}^*(\mathbf{x})\Phi(\mathbf{x} - \mathbf{x}_l)\delta x^2, \tag{26}$$

where N is the number of Lagrangian points, $\mathbf{A}$ is a $N \times N$ sparse matrix. $\mathbf{y}$ and $\mathbf{b}$ are column vectors of size N, whose elements are of size 1×2 for a two-dimensional simulation. Thus, the unknown velocity correction $\delta\mathbf{u}_l(\mathbf{x}_l)$ can be solved from

$$|\delta\mathbf{u}_l(\mathbf{x}_l)\rangle = \mathbf{A}^{-1} \left| \mathbf{u}_l(\mathbf{x}_l) - \sum_{\mathbf{x}} \mathbf{u}^*(\mathbf{x})\Phi(\mathbf{x} - \mathbf{x}_l)\delta x^2 \right\rangle. \tag{27}$$

2.3. Effect of internal mass in the IBM

In the IBM, a solid body interacting with a fluid is represented only by its surface Γ_s, and the solid interior Ω_s is filled with the same fluid. Therefore, a moving body in a fluid is actually modelled with the moving fluid inside Ω_s. For the fluid enclosed by Γ_s, the conservation of momentum shows,

$$\frac{d}{dt}\int_{\Omega_s} \rho_f \mathbf{u} dV = \int_{\Gamma_s} \mathbf{F}_l^{ib}(\mathbf{x}_l) dS + \int_{\Gamma_s} \tau \cdot \mathbf{n} dS, \tag{28}$$

where $\mathbf{n}$ is the unit outward normal vector on the solid surface Γ_s, τ is the hydrodynamic stress tensor.

For the structure immersed in a fluid, if the gravity force is neglected, the only source of external body force $\mathbf{F}_b(\mathbf{x}_s)$ in Eq. (1) is the hydrodynamic force applied on the structure surface by the surrounding fluid

$$\int_{\Omega_s} \mathbf{F}_b(\mathbf{x}_s) dV = \int_{\Gamma_s} \tau \cdot \mathbf{n} dS. \tag{29}$$

It is difficult to accurately calculate the velocity gradient at the fluid-solid interface in the IBM. Therefore, in order to avoid using the stress tensor τ in the motion equation Eq. (1), considering Eq. (28), Eq. (1) can be written in an integral form,

$$\int_{\Omega_s} \left[\rho_s \ddot{\mathbf{d}}(\mathbf{x}_s) - \mathbf{F}_{pd}(\mathbf{x}_s) \right] dV = \rho_f \frac{d}{dt} \int_{\Omega_s} \mathbf{u} dV - \int_{\Gamma_s} \mathbf{F}_l^{ib}(\mathbf{x}_l) dS. \tag{30}$$

The first term on the right-hand side of Eq. (30) is called the internal mass effect [50], which presents the momentum change of the fluid inside Ω_s.

When the no-slip boundary is successfully enforced on the fluid-solid interface Γ_s, the linear momentum of the incompressible flow in Ω_s is equal to that of the imaginary flow that follows the structure movement exactly [50], i.e.

$$\int_{\Omega_s} \mathbf{u} dV = \int_{\Omega_s} \mathbf{u}_s dV. \tag{31}$$

Although the derivation was made for a rigid body [50], it is also applicable for deformable structures. The variation of the mean velocity of the imaginary fluid in Γ_s can be expressed as,

$$\frac{d}{dt} \int_{\Omega_s} \mathbf{u}_s dV = \int_{\Omega_s} \frac{d\mathbf{u}_s}{dt} dV + \int_{\Omega_s} \mathbf{u}_s (\nabla \cdot \mathbf{u}_s) dV. \tag{32}$$

Thus, under the condition that the imaginary flow inside Ω_s is incompressible, i.e. $\nabla \cdot \mathbf{u}_s = 0$, there is the relationship as

$$\frac{d}{dt} \int_{\Omega_s} \mathbf{u} dV = \int_{\Omega_s} \ddot{\mathbf{d}}(\mathbf{x}_s) dV. \tag{33}$$

However, it must be noted that similar equality cannot be achieved for the angular momentum, which indicates the model may be less accurate if the angular

motion of the structure is more pronounced, as tested by Lācis et al. [44], Suzuki and Inamuro [50].

Substituting Eq. (33) into Eq. (30), the following equation is obtained,

$$\int_{\Omega_s} \left[(\rho_s - \rho_f)\ddot{\mathbf{d}}(\mathbf{x}_s) - \mathbf{F}_{pd}(\mathbf{x}_s) + \overline{\mathbf{F}}_l^{ib}(\mathbf{x}_s) \right] dV = 0, \tag{34}$$

where $\overline{\mathbf{F}}_l^{ib}(\mathbf{x}_s)$ is the hydrodynamic force volume density,

$$\int_{\Omega_s} \overline{\mathbf{F}}_l^{ib}(\mathbf{x}_s) dV = \int_{\Gamma_s} \mathbf{F}_l^{ib}(\mathbf{x}_l) dS. \tag{35}$$

It is assumed in Eq. (35) that the hydrodynamic force on the surface of structure is only applied on the surface layer of the structure. According to the the method of Huang et al. [51], Huang and Sung [52], the strong form of Eq. (34) is used to describe the solid motion,

$$(\rho_s - \rho_f)\ddot{\mathbf{d}}(\mathbf{x}_s) = \mathbf{F}_{pd}(\mathbf{x}_s) - \overline{\mathbf{F}}_l^{ib}(\mathbf{x}_s). \tag{36}$$

Moreover, it should be noted that the current method to alleviate the internal mass effect holds only over the solid subdomain Ω_s, as the above derivation is built upon the integration over Ω_s. By dropping the integral of Eq. (34), the internal mass effect is distributed onto the entire solid subdomain Ω_s, which means the detailed local variation of deformable structures may be affected. Meanwhile, in addition to Huang et al. [51], Huang and Sung [52], we will show in Section 3 that the current method is effective and accurate for a wide range of problems, although the impact on localised deformation needs to be fully quantified, which will be discussed in the future.

2.4. Derivation of the strong coupling scheme

In this section, the strong coupling condition on the fluid-solid interface will be presented. In the current approach, the coupling condition is applied on the surface layer of the structure, which means that the peridynamic material points located on the structure surface are tracked by the Lagrangian points of the IBM to represent the instantaneous fluid-solid interface. Using this strategy, the

communication between the material and Lagrangian points is straightforward as they are moving on the Lagrangian frames.

When the no-slip boundary is successfully enforced, the Lagrangian points of the IBM conform to these surface material points to assure the kinematic equilibrium,

$$\mathbf{x}_l = \mathbf{x}_{sf} + \mathbf{d}_{sf}, \tag{37}$$

$$\mathbf{u}_l(\mathbf{x}_l) = \mathbf{u}_{sf}, \tag{38}$$

where the surface material points are marked with the subscript sf.

For the structure immersed in a fluid, it is assumed that the hydrodynamic force acting on the surface of structure by the surrounding fluid is applied on the surface material points $\mathbf{x}_{sf}$ as indicated in Eq. (35). Therefore, the hydrodynamic force volume density in Eq. (36) is

$$\overline{\mathbf{F}}_l^{ib}(\mathbf{x}_{sf}) = \mathbf{F}_l^{ib}(\mathbf{x}_l)\frac{\delta s_l}{V_s}, \tag{39}$$

where V_s is the volume of material points. In this work, the size of material points Δ is the same as the lattice spacing δx of the CLBM, which results in $V_s = \delta x^2$. For the internal material points $\mathbf{x}_{si}$, $\overline{\mathbf{F}}_l^{ib}(\mathbf{x}_{si}) = 0$. Thus, the equation of motion for the material points $\mathbf{x}_{si}$ can be expressed as

$$(\rho_s - \rho_f)\ddot{\mathbf{d}}_{si}^n = \mathbf{F}_{pd}^n. \tag{40}$$

By substituting Eq. (7) into Eq. (8), the acceleration $\ddot{\mathbf{d}}_{sf}^n$ can be discretised as

$$\ddot{\mathbf{d}}_s^n \approx \frac{2}{\delta t^2}(\mathbf{d}_s^{n-1} + \delta t\mathbf{u}_s^n - \mathbf{d}_s^n). \tag{41}$$

Substituting Eqs. (41), (39), (27) and (21) into Eq. (36), the discretised movement equation of the surface material points $\mathbf{x}_{sf}$ can be written as

$$\begin{aligned}&\frac{2(\rho_s - \rho_f)}{\delta t^2}\left|\mathbf{d}_{sf}^{n-1} + \delta t\mathbf{u}_{sf}^n - \mathbf{d}_{sf}^n\right\rangle = \\ &\left|\mathbf{F}_{pd}^n\right\rangle - \frac{2\rho_f}{\delta t V_s}\mathrm{diag}(\delta s_l)\mathbf{A}^{-1}\left|\mathbf{u}_l^n(\mathbf{x}_l) - \sum_{\mathbf{x}}\mathbf{u}^{*n}(\mathbf{x})\Phi(\mathbf{x} - \mathbf{x}_l)\delta x^2\right\rangle,\end{aligned} \tag{42}$$

where the function $\mathrm{diag}(\delta s_l)$ is to create a diagonal matrix of size $N \times N$ with δs_l on the main diagonal. The Störmer–Verlet integration in Eqs. (7) and (8) calculates the displacement a time step ahead of the velocity term, which means $\mathbf{d}_{sf}^n$ and $\mathbf{u}_{sf}^{n-1}$ are obtained at the time step $n-1$ with Eqs. (7) and (8). Thus, $\mathbf{d}_{sf}^n$ can be used directly to update $\mathbf{A}$ and $\mathbf{F}_{pd}^n$ at the time step n. Moreover, $\mathbf{u}_l^n(\mathbf{x}_l)$ on the right-hand side of Eq. (42) can be replaced with $\mathbf{u}_{sf}^n$ according to Eq. (38). Therefore, the only unknown variable $\mathbf{u}_{sf}^n$, which guarantees the no-slip boundary condition over the fluid-solid interface, can be calculated implicitly by solving Eq. (42).

Moreover, the matrix $\mathbf{A}$ in Eq. (24) can be expressed as follows,

$$\mathbf{A} = \tilde{\mathbf{A}}\mathrm{diag}(\delta s_m), \tag{43}$$

$$\tilde{\mathbf{A}}_{lm} = \sum_{\mathbf{x}} \Phi(\mathbf{x} - \mathbf{x}_m)\Phi(\mathbf{x} - \mathbf{x}_l)\delta x^2, \tag{44}$$

and the inverse of the matrix $\mathbf{A}$ can be calculated as

$$\mathbf{A}^{-1} = \mathrm{diag}(\delta s_m^{-1})\tilde{\mathbf{A}}^{-1}. \tag{45}$$

Substituting Eq. (45) into Eq. (42), $\mathrm{diag}(\delta s_l)$ on the right-hand side of Eq. (42) can be eliminated to yield,

$$\begin{aligned} &\frac{2(\rho_s - \rho_f)}{\delta t^2}\left|\mathbf{d}_{sf}^{n-1} + \delta t \mathbf{u}_{sf}^n - \mathbf{d}_{sf}^n\right\rangle = \\ &\left|\mathbf{F}_{pd}^n\right\rangle - \frac{2\rho_f}{\delta t V_s}\tilde{\mathbf{A}}^{-1}\left|\mathbf{u}_{sf}^n - \sum_{\mathbf{x}} \mathbf{u}^{*n}(\mathbf{x})\Phi(\mathbf{x} - \mathbf{x}_l)\delta x^2\right\rangle. \end{aligned} \tag{46}$$

Then, Eq. (46) can be transformed into the linear equation,

$$\mathbf{A}^*\mathbf{y}^* = \mathbf{b}^*, \tag{47}$$

where

$$\mathbf{A}^* = \frac{\rho_s - \rho_f}{\rho_f} V_s \tilde{\mathbf{A}} + \mathbf{I}, \tag{48}$$

$$\mathbf{y}^* = \left|\mathbf{u}_{sf}^n\right\rangle, \tag{49}$$

$$\mathbf{b}^* = \frac{\rho_s - \rho_f}{\rho_f}\frac{V_x}{\delta t}\tilde{\mathbf{A}}\left|\mathbf{d}_{sf}^n - \mathbf{d}_{sf}^{n-1}\right\rangle + \frac{\delta t V_s}{2\rho_f}\tilde{\mathbf{A}}\left|\mathbf{F}_{pd}^n\right\rangle + \left|\sum_{\mathbf{x}} \mathbf{u}^*(\mathbf{x})\Phi(\mathbf{x} - \mathbf{x}_l)\delta x^2\right\rangle. \tag{50}$$

The stability condition to obtain convergent results is derived using the standard von Neumann stability analysis by assuming the displacement $\mathbf{d}_j^n$ of material point j at the time step n as

$$\mathbf{d}_j^n = \hat{\phi}^n e^{i\hat{k}j}, \tag{51}$$

where i is an imaginary number. The stability analysis requires that $|\hat{\phi}| \leq 1$ for all frequency values of $\hat{k}$. By replacing the velocity $\mathbf{u}_j$ with the displacement $\mathbf{d}_j$ according to Eqs. (7) and (8), and substituting $\mathbf{F}_{pd}^n$ with Eq. (52) below,

$$\mathbf{F}_{pd}^n = \sum_p^H c\frac{\mathbf{d}_p^n - \mathbf{d}_j^n}{|\xi|}V_p, \tag{52}$$

the strong coupling in Eq. (46) can be rewritten in the form below,

$$\begin{aligned}\tilde{\mathbf{A}}\left|\frac{\rho_s-\rho_f}{\delta t^2}(\mathbf{d}_j^{n+1}-2\mathbf{d}_j^n+\mathbf{d}_j^{n-1}) - \sum_p^H c\frac{\mathbf{d}_p^n-\mathbf{d}_j^n}{|\xi_{jp}|}V_p\right\rangle = \\ -\frac{2\rho_f}{\delta t V_s}\left|\frac{\mathbf{d}_j^{n+1}-\mathbf{d}_j^{n-1}}{2\delta t} - \sum_{\mathbf{x}}\mathbf{u}^{*n}(\mathbf{x})\Phi(\mathbf{x}-\mathbf{x}_l)\delta x^2\right\rangle.\end{aligned} \tag{53}$$

Due to the matrix $\tilde{\mathbf{A}}$ is usually a diagonally dominant pentadiagonal matrix, Eq. (53) is simplified by replacing $\tilde{\mathbf{A}}$ with $||\tilde{\mathbf{A}}||_\infty \mathbf{I}$, where $||\tilde{\mathbf{A}}||_\infty$ is the infinity norm of $\mathbf{A}$ and $\mathbf{I}$ is the unit matrix. Under the assumption of the velocity of fluid flow $\mathbf{u}^{*n} = 0$, and aided by Eq. (51), Eq. (53) becomes,

$$\alpha(\hat{\phi}^2 - \hat{\phi} + 1) - \beta\hat{\phi} = -\frac{\gamma}{2}(\hat{\phi}^2 - 1), \tag{54}$$

where

$$\alpha = \frac{\rho_s - \rho_f}{\delta t^2}||\tilde{\mathbf{A}}||_\infty, \tag{55}$$

$$\beta = c\sum_p \frac{1}{|\xi_{jp}|}(\cos(\hat{k}(p-j)) - 1)V_p||\tilde{\mathbf{A}}||_\infty, \tag{56}$$

$$\gamma = \frac{2\rho_f}{\delta t V_j}. \tag{57}$$

Enforcing the condition $|\hat{\phi}| \leq 1$ to the solutions of Eq. (54) for all $\hat{k}$ values

results in

$$\delta t < \sqrt{\frac{2(\rho_s - \rho_f)}{c\sum_p |\xi_{jp}|^{-1}}}, \tag{58}$$

$$\rho_s > \rho_f. \tag{59}$$

Since there is always $|\xi_{jp}| \geq \Delta$ in the peridynamic simulations, the critical time step δt_c for a two-dimensional simulation can be estimated by

$$\delta t_c = \sqrt{\frac{2(\rho_s - \rho_f)}{c\pi\delta^2}}. \tag{60}$$

2.5. The relaxed multi-direct-forcing scheme

Eq. (47) needs to be solved to obtain the unknown velocity $\mathbf{u}_{sf}^n$. It should be pointed out that a direct solution of Eq. (47) requires to calculate the inverse of the matrix $\mathbf{A}^*$, which is computationally expensive. In our simulations, the Lagrangian points track the moving fluid-solid interface, which means the matrix $\mathbf{A}^*$ is time-varying and its inverse need to be updated at every time step. Therefore, the direct solution is not an efficient choice.

Our previous paper [22] demonstrated that the relaxed MDF scheme, which is based on the relaxed Richardson iteration, not only avoids the calculation of matrix inverse, but also improves the efficiency and accuracy of the traditional MDF scheme. The relaxed MDF scheme is implemented following the two steps: firstly, the relaxed Richardson iteration equation is obtained from the original linear system and a relaxation parameter is determined; secondly, the iteration is performed through the interpolation and distribution operations as described by Eqs. (17) and (20).

To ensure the convergence of the Richardson iteration, the matrix $\mathbf{A}^*$ should be positive-definite and symmetric, which is the case for matrix $\tilde{\mathbf{A}}$ according to Eq. (44). Since $\rho_s > \rho_f$ in our simulations, $\mathbf{A}^*$ calculated from Eq. (48) shares the same characteristics as $\tilde{\mathbf{A}}$. Therefore, Eq. (47) can be solved with the relaxed Richardson equation as follows,

$$\mathbf{y}^{*k+1} = (\mathbf{I} - \omega\mathbf{A}^*)\,\mathbf{y}^{*k} + \omega\mathbf{b}^*, \tag{61}$$

where ω is the relaxation parameter and k is the iteration counter. To accelerate the convergence rate, the relaxation parameter ω can be set as

$$\begin{aligned} \omega &= ||\mathbf{A}^*||_\infty^{-1}, \\ ||\mathbf{A}^*||_\infty &= \frac{\rho_s - \rho_f}{\rho_f} V_s ||\tilde{\mathbf{A}}||_\infty + 1. \end{aligned} \tag{62}$$

It is straightforward to solve Eq. (23) with the interpolation and distribution operations in Eqs. (17) and (20) as matrix $\mathbf{A}$ is formed by a combination of these two operations (see Eq. (24)). However, $\mathbf{A}^*$ and $\mathbf{b}^*$ in Eq. (61) are more complicated than $\mathbf{A}$ and $\mathbf{b}$ in Eq. (23). Thus, the strategy of implementing the relaxed MDF scheme should be modified accordingly to solve the new strong coupling equation, i.e Eq. (46) efficiently.

By substituting Eq. (48) into Eq. (61), $\mathbf{y}^{*k+1}$ can be expressed as

$$\mathbf{y}^{*k+1} = (1-\omega)\mathbf{y}^{*k} + \omega \left(\mathbf{b}^* - \frac{\rho_s - \rho_f}{\rho_f} V_s \tilde{\mathbf{A}} \mathbf{y}^{*k} \right). \tag{63}$$

Then, substituting Eq. (50) for $\mathbf{b}^*$ in Eq. (63) yields

$$\begin{aligned} \mathbf{y}^{*k+1} =& (1-\omega)\mathbf{y}^{*k} + \omega \left| \sum_{\mathbf{x}} \mathbf{u}^*(\mathbf{x}) \Phi(\mathbf{x} - \mathbf{x}_l) \delta x^2 \right\rangle + \\ & \omega \tilde{\mathbf{A}} \left[\frac{\rho_s - \rho_f}{\rho_f} \frac{V_s}{\delta t} \left(\left| \mathbf{d}_{sf}^n - \mathbf{d}_{sf}^{n-1} \right\rangle - \mathbf{y}^{*k} \delta t \right) + \frac{\delta t V_s}{2\rho_f} \left| \mathbf{F}_{pd}^n \right\rangle \right]. \end{aligned} \tag{64}$$

By substituting Eq. (27) into Eq. (42), the following relationship between $\delta \mathbf{u}_l^n(\mathbf{x}_l)$ and $\mathbf{u}_{sf}^n$ is obtained,

$$\mathrm{diag}(\delta s_l) \left| \delta \mathbf{u}_l^n(\mathbf{x}_l) \right\rangle = \frac{\rho_s - \rho_f}{\rho_f} \frac{V_s}{\delta t} \left| \mathbf{d}_{sf}^n - \mathbf{u}_{sf}^n \delta t - \mathbf{d}_{sf}^{n-1} \right\rangle + \frac{\delta t V_s}{2\rho_f} \left| \mathbf{F}_{pd}^n \right\rangle, \tag{65}$$

which can be rearranged to make it suitable for an iterative scheme as follows,

$$\mathrm{diag}(\delta s_l) \left| \delta \mathbf{u}_l^{n,k}(\mathbf{x}_l) \right\rangle = \frac{\rho_s - \rho_f}{\rho_f} \frac{V_s}{\delta t} \left(\left| \mathbf{d}_{sf}^n - \mathbf{d}_{sf}^{n-1} \right\rangle - \mathbf{y}^{*k} \delta t \right) + \frac{\delta t V_s}{2\rho_f} \left| \mathbf{F}_{pd}^n \right\rangle. \tag{66}$$

Finally, by substituting Eq. (66) and Eq. (43) into Eq. (64), there is the relationship

$$\mathbf{y}^{*k+1} = (1-\omega)\mathbf{y}^{*k} + \omega \left[\mathbf{A} \left| \delta \mathbf{u}_l^{n,k}(\mathbf{x}_l) \right\rangle + \left| \sum_{\mathbf{x}} \mathbf{u}^*(\mathbf{x}) \Phi(\mathbf{x} - \mathbf{x}_l) \delta x^2 \right\rangle \right], \tag{67}$$

where the interpolation and distribution operations can be expanded from the matrix $\mathbf{A}$ as follows,

$$\mathbf{u}_{sf}^{n,k+1} = (1-\omega)\mathbf{u}_{sf}^{n,k} + \omega \sum_{\mathbf{x}} \left[\mathbf{u}^*(\mathbf{x}) + \sum_{\mathbf{x}_m} \delta\mathbf{u}_l^{n,k}(\mathbf{x}_m)\Phi(\mathbf{x}-\mathbf{x}_m)\delta s_m \right] \Phi(\mathbf{x}-\mathbf{x}_l)\delta x^2. \tag{68}$$

Therefore, Eq. (47) can be solved iteratively using Eqs. (66) and (68).

In Eqs. (66) and (68) the unrefined velocity $\mathbf{u}^*(\mathbf{x})$ should always be stored for the iterations. To reduce memory consumption during the simulation, the cumulative correction procedure used by Zhang et al. [22] is employed. First, Eq. (66) is modified as follows,

$$\Delta\mathbf{u}_l^{n,k} = -\frac{\rho_s - \rho_f}{\rho_f \delta t}\frac{V_s}{\delta s_l}(\mathbf{u}_{sf}^{n,k} - \mathbf{u}_{sf}^{n,k-1}), \tag{69}$$

where

$$\Delta\mathbf{u}_l^{n,k} = \delta\mathbf{u}_l^{n,k} - \delta\mathbf{u}_l^{n,k-1}, \tag{70}$$

$$\Delta\mathbf{u}_l^{n,0} = \frac{\rho_s - \rho_f}{\rho_f \delta t}\frac{V_s}{\delta s_l}\left(\mathbf{d}_{sf}^{n} - \mathbf{d}_{sf}^{n-1} - \mathbf{u}_{sf}^{n,0}\delta t\right) + \frac{\delta t}{2\rho_f}\frac{V_s}{\delta s_l}\mathbf{F}_{pd}^{n}. \tag{71}$$

Then, Eq. (68) is transformed into a cumulative form to eliminate $\mathbf{u}^*(\mathbf{x})$,

$$\mathbf{u}_{sf}^{n,k+1} = (1-\omega)\mathbf{u}_{sf}^{n,k} + \omega \sum_{\mathbf{x}} \left[\mathbf{u}^{n,k}(\mathbf{x}) + \sum_{\mathbf{x}_m} \Delta\mathbf{u}_l^{n,k}(\mathbf{x}_m)\Phi(\mathbf{x}-\mathbf{x}_m)\delta s_m \right] \Phi(\mathbf{x}-\mathbf{x}_l)\delta x^2, \tag{72}$$

where

$$\mathbf{u}^{n,k}(\mathbf{x}) = \mathbf{u}^*(\mathbf{x}) + \sum_{\mathbf{x}_m} \delta\mathbf{u}_l^{n,k-1}(\mathbf{x}_m)\Phi(\mathbf{x}-\mathbf{x}_m)\delta s_m, \tag{73}$$

$$\mathbf{u}^{n,0}(\mathbf{x}) = \mathbf{u}^*(\mathbf{x}). \tag{74}$$

The cumulative iteration in Eqs. (69) and (72) can be conducted following

the steps below,

$$\text{Distribution: } \Delta\mathbf{u}^k(\mathbf{x}) = \sum_{\mathbf{x}_l} \Delta\mathbf{u}_l^k(\mathbf{x}_l)\Phi(\mathbf{x}-\mathbf{x}_l)\delta s_l, \tag{75}$$

$$\mathbf{u}^{k+1}(\mathbf{x}) = \mathbf{u}^k(\mathbf{x}) + \Delta\mathbf{u}^k(\mathbf{x}); \tag{76}$$

$$\text{Interpolation: } \mathbf{u}^{k+1}(\mathbf{x}_l) = \sum_{\mathbf{x}} \mathbf{u}^{k+1}(\mathbf{x})\Phi(\mathbf{x}-\mathbf{x}_l)\delta x^2, \tag{77}$$

$$\mathbf{u}_{sf}^{k+1} = (1-\omega)\mathbf{u}_{sf}^k + \omega\mathbf{u}^{k+1}(\mathbf{x}_l), \tag{78}$$

$$\Delta\mathbf{u}_l^{k+1} = -\frac{\rho_s-\rho_f}{\rho_f}\frac{V_s}{\delta s_l}(\mathbf{u}_{sf}^{k+1}-\mathbf{u}_{sf}^k), \tag{79}$$

$$\mathbf{F}_{ib,l}^{k+1}(\mathbf{x}_l) = \mathbf{F}_{ib,l}^k(\mathbf{x}_l) + \frac{2\rho_f}{\delta t}\Delta\mathbf{u}_l^{k+1}(\mathbf{x}_l); \tag{80}$$

where $\mathbf{F}_{ib,l}^0(\mathbf{x}_l)$ is zero and $\mathbf{u}_{sf}^0$ is calculated with Eq. (40). The strong coupling interface is achieved by adding velocity corrections simultaneously for the fluid and solid with Eqs. (76) and (78), respectively. After the cumulative iterations described by Eqs. (75)–(80) are concluded, the last velocity correction $\Delta\mathbf{u}_l$ is distributed to the nearby fluid domain according to Eqs. (75) and (76). Then the hydrodynamic force on the IB points $\mathbf{F}_l^{ib}(\mathbf{x}_l)$ is distributed to the fluid domain to finalise the iteration,

$$\mathbf{F}^{ib}(\mathbf{x}) = \sum_{\mathbf{x}_l} \mathbf{F}_l^{ib}(\mathbf{x}_l)\Phi(\mathbf{x}-\mathbf{x}_l)\delta s_l. \tag{81}$$

2.6. The computational algorithm

The algorithm of the strong coupling partitioned approach is summarised as follows:

1. Flow solver: CLBM
   (a) Perform the fluid evolution according to Eq. (9);
   (b) Calculate the macroscopic fluid variables using Eqs. (13) and (14).
2. Solid solver: Peridynamic model
   (a) Calculate the internal forces $\mathbf{F}_{pd}^n$ according to Eq. (2);
   (b) Obtain the displacement and velocity of all the material points $\mathbf{d}_s^{n+1}$ and $\mathbf{u}_s^n$ using Eqs. (40), (7) and (8).
3. Update the locations of Lagrangian points $\mathbf{x}_l^n$ according to Eq. (37).

4. The strong coupling interface: the relaxed MDF-IBM
   (a) Calculate the matrix $\tilde{\mathbf{A}}$ with Eq. (44), then update the relaxation parameter ω according to Eq. (62);
   (b) Set $k = 0$, $\mathbf{u}^0(\mathbf{x}) = \mathbf{u}^*(\mathbf{x})$, $\mathbf{F}^0_{ib,l}(\mathbf{x}_l) = 0$, and calculate $\Delta\mathbf{u}^0_l(\mathbf{x}_l)$ using Eq. (71);
   (c) Perform the distribution operation as described by Eqs. (75) and (76);
   (d) Perform the interpolation operation using Eqs. (77)–(80);
   (e) Advance k to $k+1$ and repeat Steps 4c-4d while $k < L_m$, where L_m is the total number of iterations;
   (f) Distribute the last velocity correction $\Delta\mathbf{u}^n_l$ to the fluid domain as described by Eqs. (75) and (76);
   (g) Distribute the surface force $\mathbf{F}^n_{ib,l}(\mathbf{x}_l)$ to the fluid domain using Eq. (81).
5. Update the location and velocity of material points $\mathbf{d}^{n+1}_{sf}$, $\mathbf{u}^n_{sf}$ with the obtained $\mathbf{F}^n_{ib,l}$.
6. Advance the time step to $n+1$, and repeat Steps 1-5.

As shown above, the fluid and solid solvers are launched only once at Steps 1 and 2 respectively in a single time step, and the strong coupling interface is solved iteratively with the relaxed MDF-IBM at Step 4.

3. Numerical examples

3.1. Plate with a pre-existing crack under velocity boundary conditions

In this section, the behaviour of a two-dimensional plate with a pre-existing crack is simulated to validate the peridynamic model for structural deformation and crack capture. As shown in Fig. 1, the length and the width of the plate are respectively $L = 50$ mm and $W = 50$ mm, and the origin of coordinates xOy is at the bottom left corner of the plate. A horizontal crack of length $D = 10$ mm is initialized in the centre of the plate. The plate is discretized with 500×500 material points. The plate is subjected to velocity boundary conditions along its upper and bottom edges, $U_y = \pm 20$ m/s. The velocity boundary condition

is applied at two additional boundary layers R_c as shown in Fig. 1. There are 500×3 material points over each boundary layer R_c. The material properties of the plate include the Young's modulus $E = 192$ GPa, Poisson's ratio $\nu = 0.33$, solid density $\rho_s = 8000$ kg/m^3. The time step is $\delta t = 1.3367 \times 10^{-8}$ s.

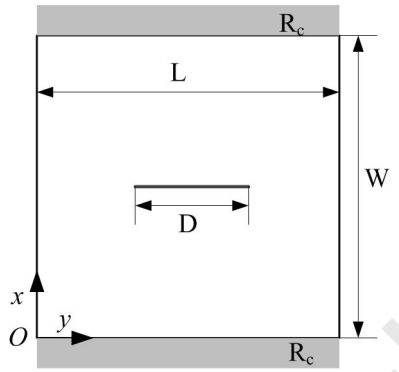

Figure 1: The schematic of a plate with a pre-existing crack.

Firstly, the breakage of bonds between material points is not allowed. Under the stretching of upper and bottom boundaries, the crack opens gradually and forms an ellipse-like shape. The displacement of material points near the initial horizontal crack at the time $t = 16.7$ μs is plotted in Fig. 2. The results match well with those from Madenci and Oterkus [11]. Then, crack generation is allowed by using the critical stretch $s_c = 0.04472$. The initial crack keeps growing toward the left and right boundaries of the plate as shown in Fig. 3. The horizontal location of the right tip of the growing crack is recorded in Fig. 4 which is in good agreement with the results of Madenci and Oterkus [11].

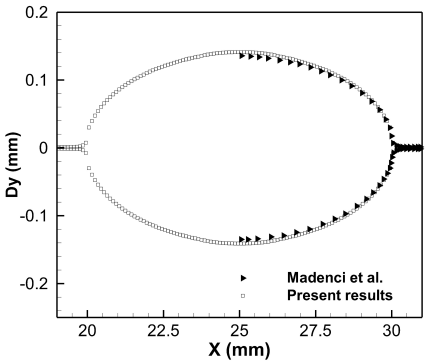

Figure 2: Vertical displacement D_y of the material points near the initial crack at the time $t = 16.7$ μs when failure is not allowed.

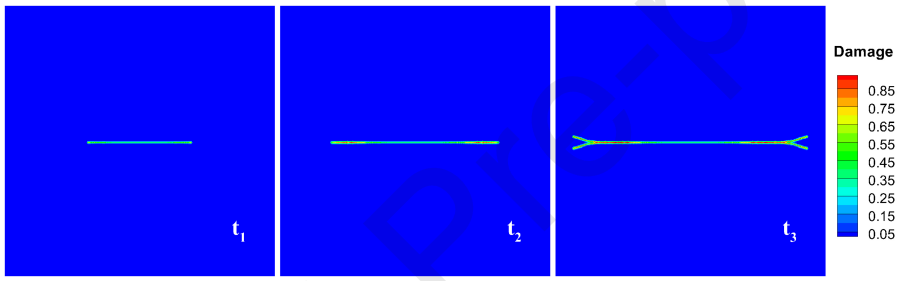

Figure 3: Crack growth at three instants, $t_1 = 10.0$ μs, $t_2 = 13.4$ μs, $t_3 = 16.7$ μs, when failure is allowed.

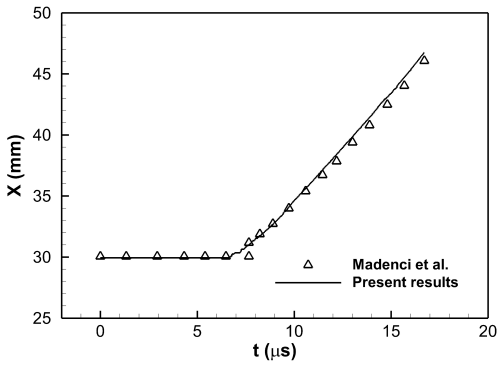

Figure 4: Variation of the horizontal location X of the right tip of the growing crack when failure is allowed. Damage here is quantified as the ratio of the number of broken bonds to the total number of bonds for each peridynamic material point.

3.2. Sedimentation of an elastic disk under gravity

An elastic circular disk placed in a viscous fluid falls freely under gravity g of 980 cm/s^2 as sketched in Fig 5. The diameter of the disk D is 0.25 cm. The density of fluid ρ_f is 1.0 g/cm^3. The kinematic viscosity of fluid ν_f is 1.0 cm^2/s. The width and height of the computational domain are $W = 2.0$ cm and $H = 5.0$ cm, respectively. A no-slip boundary is applied at all the four edges and a fixed reference pressure $p = 0$ at the upper boundary. Initially, both the velocities of fluid and solid are set to be zero, the initial pressure of the fluid is $p = 0$, and the distance between the disk centre and the upper boundary L is 1.0 cm. The number of lattices over the disk diameter is 100, which corresponds to $\delta x = 2.5 \times 10^{-3}$ cm. The Poisson's ratio for the disk ν_s is 0.33. The solid density ρ_s is larger than the fluid density ρ_f so that the disk can move downwards under the gravity and buoyancy forces. In addition, the performance of the current method as ρ_s approaches to ρ_f will be demonstrated in this case.

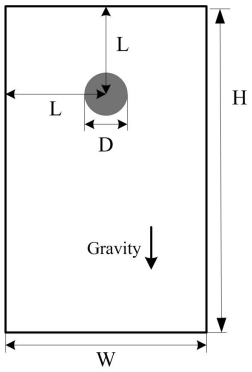

Figure 5: A schematic of the sedimentation of a disk under gravity.

The sedimentation of a circular disk with different densities $\rho_s = (1.05, 1.1, 1.5, 2.0)\rho_f$ and the Young's modulus $E = 1 \times 10^4$ g/(cm·s^2) is simulated to validate the ability of the present numerical scheme for the cases with a density ratio close to unity. The variation of the vertical velocity of the disk V_y is recorded in Fig. 6. Meanwhile, as the scheme of Feng and Michaelides [53] can compensate the internal mass effect of rigid objects, which has been verified by multiple publications [21, 50, 53], the vertical velocity variation of a rigid circular disk is also presented for assessing the current approach to mitigating the internal mass effect. It can be seen in Fig. 6 that for both rigid and elastic disks the settling velocity keeps increasing until it reaches the stable terminal velocity V_t. The specific values of V_t are displayed in Table 2, where the empirical results are calculated using the following equation [54]:

$$V_t = \frac{(\rho_s - \rho_f)gR^2}{4\rho_f \nu_f}\left[\ln\left(\frac{W}{D}\right) - 0.9157 + 1.7244\left(\frac{D}{W}\right)^2 - 1.7302\left(\frac{D}{W}\right)^4\right].$$

It is clear that the terminal velocities of both rigid and elastic disks agree well with the empirical results.

By comparing the movement of the rigid disk with and without compensating the internal mass effect, i.e. the lines noted by "InM" and "No InM" respectively in Fig. 6, it can be found that the internal mass effect is pronounced in the acceleration phase as stated by Suzuki and Inamuro [50]. Throughout both

the acceleration phase and the steady falling phase, the movement of the elastic disk simulated by the current method agrees well with that of the rigid disk (InM), for which the internal mass effect is dealt with appropriately. Specifically, for the case with $\rho_s = 2.0\rho_f$ and a larger Young's modulus $E = 1 \times 10^8$ g/(cm·s^2), which means the elastic particle is more rigid, the variation of the vertical velocity is almost identical to that of the rigid disk (InM). Thus, for the case with insignificant particle rotation, the current method for minimizing the internal mass effect is appropriate. For the elastic disk with a small solid density ρ_s and a small Young's modulus E, a relatively significant oscillation during the acceleration phase is observed, which was not reported in any previous computational or experimental study. This may be caused by the spurious stress computation in the immersed boundary method, and further study will be needed to understand and mitigate the unphysical oscillations under small solid density and Young's modulus.

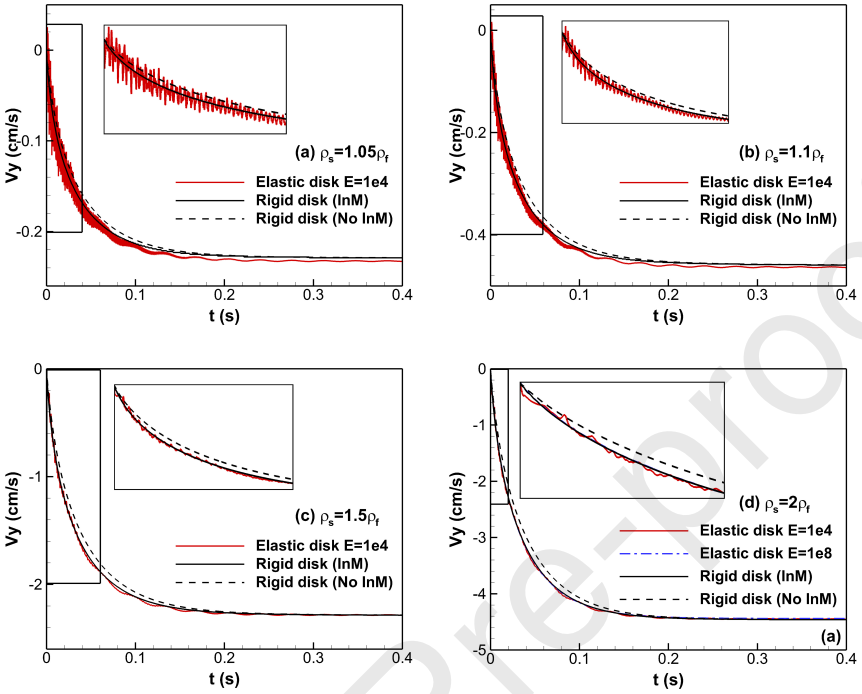

Figure 6: Variations of the vertical velocity of the disk V_y: (a) $\rho_s = 1.05\rho_f$; (b) $\rho_s = 1.1\rho_f$; (c) $\rho_s = 1.5\rho_f$; and (d) $\rho_s = 2.0\rho_f$.

Table 2: Terminal vertical velocity V_t of different disks at $t = 0.4$ s.

ρ_s/ρ_f	Rigid Disk		Elastic Disk
	Empirical Equation [54]	InM [53]	$E = 1 \times 10^4$
1.05	-0.228	-0.229	-0.233
1.1	-0.456	-0.459	-0.464
1.5	-2.278	-2.285	-2.286
2	-4.556	-4.461	-4.454

The contours of the velocity and vorticity fields near the disk with $E = 1{\times}10^4$ g/(cm·s^2) and $\rho_s = 2.0\rho_f$ are presented in Fig. 7. The influence of the number

of iterations L_m of the relaxed MDF scheme is investigated by employing $L_m =$ 1, 2, and 5 for the case in Fig. 7. To assess the accuracy of the no-slip boundary at the fluid-solid interface quantitatively, the dimensionless numerical boundary error is defined as

$$Er = \frac{1}{N} \frac{\sum_N ||\mathbf{u}_{sf}^n - \mathbf{u}^n(\mathbf{x}_l)||}{||V_t||}, \tag{82}$$

where $\mathbf{u}^n(\mathbf{x}_l)$ is the fluid velocity interpolated using Eq. (17), $\mathbf{u}_{sf}^n$ is the velocity of the surface material points obtained after L_m iterations. It can be seen from Table 3 that the difference between V_y values in the cases with $L_m = 1$ and $L_m = 5$ is only 0.6%, and the numerical boundary error Er drops by 78% when L_m increases from 1 to 5. It is clear that the relaxed MDF scheme works well to solve Eq. (47) efficiently.

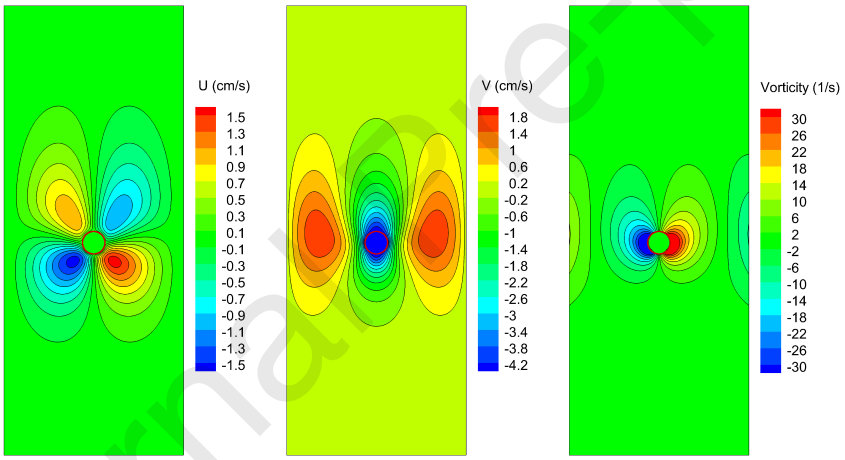

Figure 7: Contours of the horizontal velocity U, the vertical velocity V, and the vorticity of the flow field at time $t = 0.4$ s.

Table 3: The influence of the number of iterations L_m on the convergence of the relaxed MDF scheme.

Iteration times L_m	1	2	5
Terminal vertical velocity V_y (cm/s)	-4.456	-4.454	-4.450
Numerical boundary error Er	3×10^{-4}	1.35×10^{-4}	6.55×10^{-5}

3.3. Cross-flow over a deformable beam

A deformable beam is fixed at the bottom of the channel filled with a viscous fluid as illustrated in Fig. 8, where Point A represents the tip of the beam. The fluid and the beam are at rest initially. Then the beam starts to deform and bend toward the outlet boundary when the fluid moves in at the inlet. The length and height of the computational domain are $L = 4$ cm and $H = 1$ cm, respectively. The thickness and height of the beam are $a = 0.04$ cm and $b = 0.8$ cm, respectively. The influence of gravity and buoyancy is ignored here. The half-way bounce back boundary condition is applied at the bottom edge and the symmetrical boundary condition at the top edge. At the inlet boundary, the velocity profile is prescribed as $u = 1.5(-y^2 + 2y)$ cm/s and $v = 0$, and at the outlet boundary a constant pressure $p = 0$ is imposed. The density and dynamic viscosity of the fluid are $\rho_f = 1.0$ g/cm^3 and $\mu_f = 0.1$ g/(cm·s), respectively. The density, Young's modulus and Poisson's ratio of the beam are set to be $\rho_s = 7.8$ g/cm^3, $E = 10^5$ g/(cm·s^2) and $\mu_s = 0.33$, respectively.

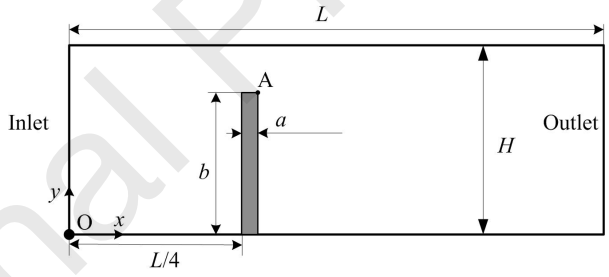

Figure 8: A schematic of the deformable beam in a cross flow.

In the simulations presented in Fig. 9, the beam is discretised using $(5 \times 103, 10 \times 203, 20 \times 403, 40 \times 803)$ material points to yield different material point sizes, i.e. $\delta x = (1, 2, 4, 8) \times 10^{-3}$ cm, respectively. The numbers of Lagrangian points tracking the fluid-solid interface for different spatial resolutions are 203, 408, 818, 1638, respectively. The bottom end of the beam with a height of $3\delta x$ is fixed and placed below the bottom boundary of the computation domain to impose a velocity constraint. With the time step $\delta t = 2 \times 10^{-6}$ s and the iterative

times of the relaxed MDF scheme $L_m = 2$, the horizontal movement of Point A against time t is shown in Fig. 9. The horizontal displacement of Point A, i.e. D_x in Fig. 9a, indicates the bending magnitude of the beam. It shows that the tip of the beam firstly bends toward the outlet boundary and then springs back a little to an equilibrium location. As shown in Fig. 9, the horizontal displacement and velocity of Point A are in a good agreement with the results reported by Han et al. [55], where an Eulerian-Lagrangian-Lagrangian method designed for FSI problems with thin structures was employed.

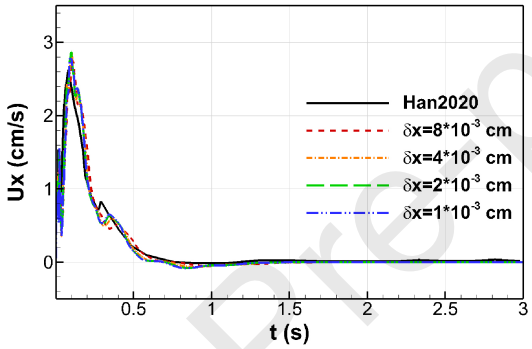

(a) The horizontal velocity, U_x.

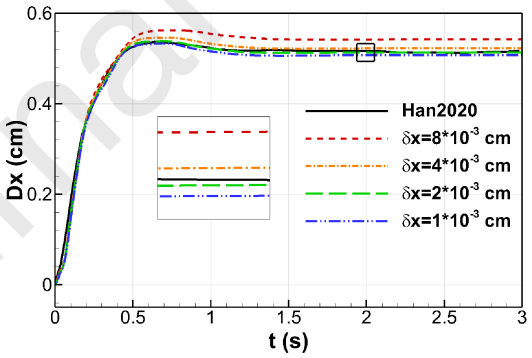

(b) The horizontal displacement, D_x.

Figure 9: The time history of the horizontal motion of Point A. The results are compared with the benchmark values presented by Han et al. [55].

The horizontal displacement of Point A at the time $t = 3.0$ s is also recorded

in Table 4. Different from Han et al. [55], the current method with a coarse meshing can result in a more significant bending. As the grid resolution increases, the influence of δx becomes smaller. In addition, to study the temporal convergence of the current method, four different time steps ($\delta t = (2, 4, 8, 16) \times 10^{-6}$ s), are also presented in Table 4 with $\delta x = 2 \times 10^{-3}$ cm. A finer temporal resolution produces a slightly larger horizontal displacement. These results indicate that the current method converges with a refined spatial and temporal resolution.

Table 4: Horizontal displacement of Point A at $t = 3.0$ s for different δt and δx.

$\delta t = 2 \times 10^{-6}$ s				
δx (10^{-3} cm)	8	4	2	1
D_x (cm)	0.5421	0.5225	0.5131	0.5073
$\delta x = 2 \times 10^{-3}$ cm				
δt (10^{-6} s)	16	8	4	2
D_x (cm)	0.5089	0.5112	0.5124	0.5131

With $\delta t = 2 \times 10^{-6}$ s, $\delta x = 2 \times 10^{-3}$ cm and $L_m = 2$, the contours of the horizontal velocity and the pressure of the fluid domain at different instants ($t = (0.1, 0.8, 3.0)$ s) are presented in Figs. 10 and 11. The streamlines of the flow at $t = 3.0$ s in Fig. 12 show that the cross-flow is blocked successfully by the bending beam and a stable recirculation zone appears in the downside of the beam.

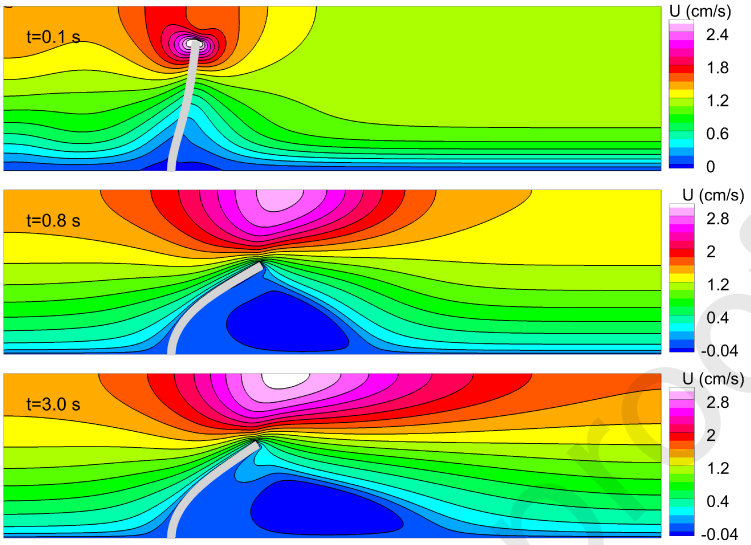

Figure 10: Horizontal velocity contour of the flow at three instants, i.e. $t = (0.1, 0.8, 3.0)$ s.

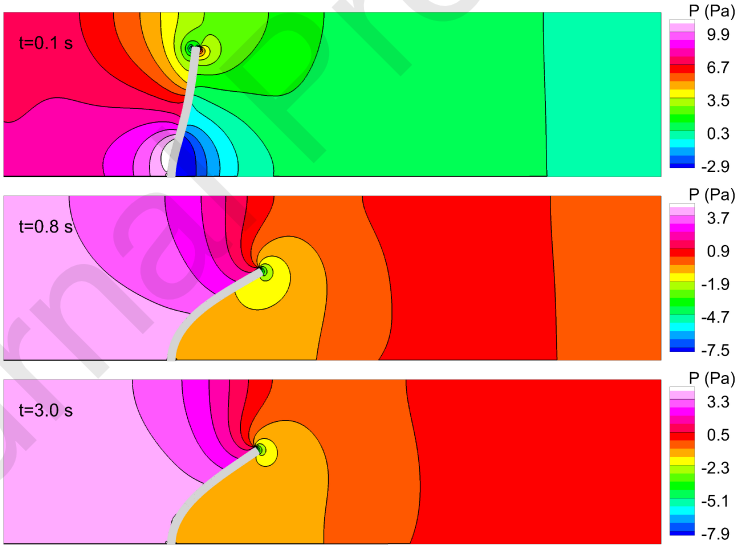

Figure 11: Pressure contour of the flow field at three instants, i.e. $t = (0.1, 0.8, 3.0)$ s.

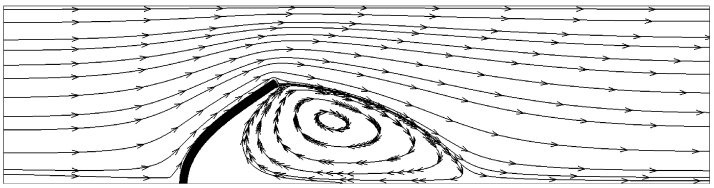

Figure 12: Streamlines of the flow field when the beam deformation and flow reach a steady state at $t = 3$ s.

The dynamic deformation and fracture of the beam under the hydrodynamic force are presented in Fig. 13. For different critical bond stretches, i.e. $s_c = 0.02, 0.1$, the corresponding fracture energies are $G_c = (0.173, 4.32) \times 10^{-3}$ J/m^2, respectively. A smaller s_c means that the material damage happens more quickly under the same loading, so Fig. 13a shows that the beam with $s_c = 0.02$ experiences a complete rupture, while Fig. 13b shows only slight damage at the bottom left corner of the beam with $s_c = 0.1$. According to the vector plot at the time $t = 0.56$ s as shown in Fig. 13a, the ruptured beam cannot block the flow and instead moves with the flow. This demonstrates the advantages of the current strong coupling approach clearly: firstly, the beam bending and its interaction with the fluid are correctly captured; secondly, the coupling with the peridynamic model also allows us to predict crack formation and propagation in the beam as well as breakup of the beam.

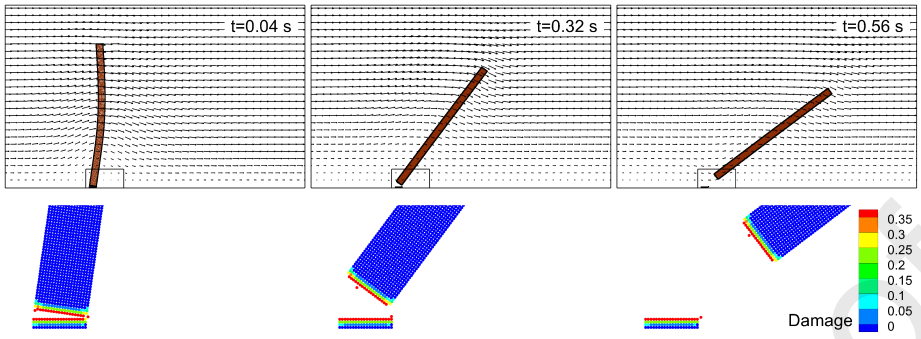

(a) $s_c = 0.02$

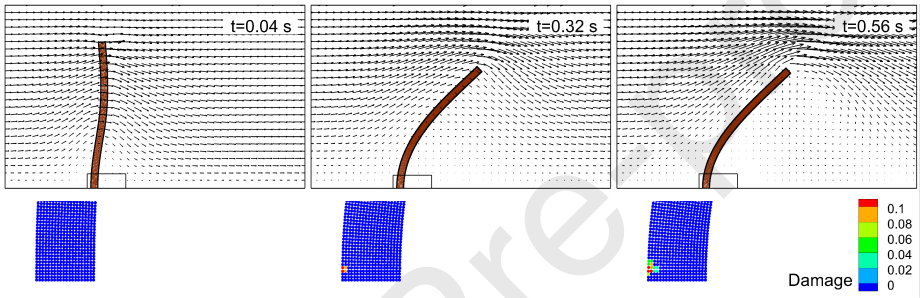

(b) $s_c = 0.1$

Figure 13: Crack formation and breakup (indicated by the damage of peridynamic material points) of the bent beam with different critical bond stretches $s_c = 0.02, 0.1$, and the corresponding vector plots of the fluid presented at $t = 0.04, 0.32, 0.56$s. Damage here is quantified as the ratio of the number of broken bonds to the total number of bonds for each peridynamic material points.

3.4. The flow-induced deformation of an elastic beam attached to a cylinder

The flow-induced deformation of an elastic beam attached to a rigid cylinder was originally considered by Turek and Hron [56]. The problem is widely used as a benchmark example to test the numerical schemes for fluid-flexible structure interaction problems [56–59]. The initial configuration of the problem is shown in Fig. 14. The elastic beam of size $(3.5D, 0.2D)$ is attached to a fixed rigid circular cylinder with the diameter $D = 0.1$ m. The size of the computational domain is $L \times W = 25D \times 4.1D$. The structure made up of the cylinder and beam is placed asymmetrically. The no-slip boundary condition is applied for

the upper and bottom boundaries, and the zero-gradient boundary condition for the outlet. At the inlet boundary, the parabolic inflow velocity profile is prescribed as $U_{in} = 1.5\bar{U}y/W(1 - y/W)$, where $\bar{U}$ is the mean velocity.

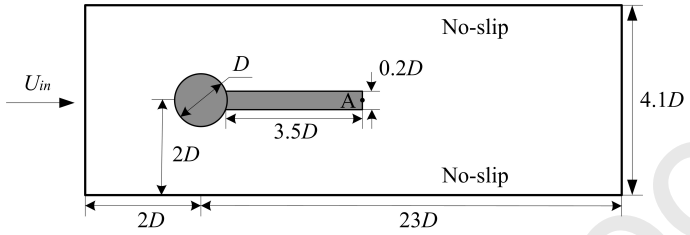

Figure 14: Initial configuration of the vortex-induced vibration of a deformable beam.

The density and kinematic viscosity of the fluid are $\rho_f = 1.0 \times 10^3$ kg/m^3 and $\nu_f = 0.001$ m^2/s, respectively. The physical properties of the beam include the density ρ_s, the Young's modulus E, and the Poisson's ratio ν. For the bond-based peridynamic model, the Poisson's ratio ν is always 0.33. The Reynolds number is defined as $Re = \bar{U}D/\nu$ in the simulations. The cases of Turek and Hron [56] are considered in this work, (1) FSI1: $\rho_s = 1.1\rho_f$, $E = 1.4 \times 10^6$ Pa, $Re = 20$; (2) FSI2: $\rho_s = 10\rho_f$, $E = 1.4 \times 10^6$ Pa, $Re = 100$; (3) FSI3: $\rho_s = 1.1\rho_f$, $E = 5.6 \times 10^6$ Pa, $Re = 200$. It should be noted that due to the density ratio limitation, i.e. $\rho_s/\rho_f > 1$, in the current method, the solid density ratio $\rho_s/\rho_f = 1.1$ in FSI1 and FSI3 is chosen to be close to 1.0 used by Turek and Hron [56]. There are 100 lattices over the diameter of the rigid cylinder. As the size of peridynamic points is the same as that of lattices of the CLBM in this work, i.e. $\Delta = \delta x$, the number of material points to discretize the beam is 353×20. The left end of the beam with the length $3\delta x$ is extended into the cylinder to ensure a fixed left end for the beam. The distribution of Lagrangian points on the jointed structure is displayed in Fig. 15. The Lagrangian points along the cylinder surface are distributed evenly and the spacing δs is close to δx ($\delta s \approx 0.997\delta x$). The time steps δt for the cases of FSI1, FSI2, and FSI3 are $(2.5, 1.25, 1.25)\times 10^{-6}$ s, respectively.

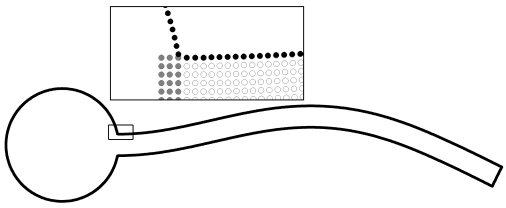

Figure 15: The distribution of Lagrangian points on the structure's surface. The Lagrangian points are denoted by the symbol ● and the peridynamic material points by ○. Furthermore, the material points inside the cylinder are marked by ◉.

As the fluid passes through the fixed cylinder, the attached flexible beam will deform. For a large Reynolds number, there will be vortexes shedding at the wake of the cylinder, so the beam is expected to oscillate periodically. The growth and oscillation of the beam deformation can be witnessed in Fig. 16, where D_y is the vertical displacement of Point A. Moreover, the influence of the internal mass is clearly demonstrated by comparing the results with and without compensating the internal mass effect, see the results denoted by InM and No InM in Fig. 16. It can be seen that for FSI1 the beam firstly deflects downward slightly and then moves upwards until becoming steady at the location $D_y = 0.9376$ mm. Point A of the case FSI1 reaches a steady terminal location which is hardly affected by the internal mass effect, apart from a slight discrepancy at $t \approx 3.1$s. On the other hand, for FS2 and FSI3, the influence of the internal mass effect is significant and continuous, lasting from the early-stage deformation growth to the final periodic oscillation.

Table 5 shows the detailed comparison of the displacements D_x and D_y of Point A in FSI1, FSI2, and FSI3 with the results published by Turek and Hron [56] and Kollmannsberger et al. [59]. The displacement is given in the form of "$<$ Mean $> \pm <$ Amplitude $><$ Frequency (Hz) $>$", where the mean value is $(D_{max} + D_{min})/2$, the amplitude is $(D_{max} - D_{min})/2$, and the frequency is obtained with a Fourier transformation of D_x and D_y. It seems that when the internal mass effect is considered (InM) in the current method, an excellent agreement is achieved in all the three cases despite the slight difference in ρ_s.

When the internal mass effect is not considered (No InM), the results of FSI1 show little difference, while for FSI2 and FSI3, the reductions in the frequency of D_y are 10.5% and 9.3%, respectively, and the increases in the amplitude of D_y are 9.7% and 23.0%, respectively. The periodical movement of Point A is compared in detail with the results from Turek and Hron [56] in Fig. 17. It is obvious that the influence of the internal mass is much more significant for FSI3 ($Re = 200$) than for FSI2 ($Re = 100$). These results are consistent with the conclusion drawn by Suzuki and Inamuro [50] for unsteady body motions, i.e. the internal mass effect becomes more and more pronounced as the Reynolds number increases.

Table 5: The displacement of Point A in comparison with the previously reported data.

FSI1	D_x (10^{-3} m)	D_y (10^{-3} m)
Turek and Hron [56]	0.0227	0.8209
Kollmannsberger et al. [59]	0.0229	0.810
Current method (InM)	0.0159	0.9376
Current method (No InM)	0.0078	0.9350
FSI2	D_x (10^{-3} m)	D_y (10^{-3} m)
Turek and Hron [56]	-14.58 ± 12.44[3.8]	1.23 ± 80.6[2.0]
Kollmannsberger et al. [59]	-15.1 ± 12.8[3.8]	1.20 ± 83.4[1.9]
Current method (InM)	-15.6 ± 12.9[3.5]	1.28 ± 84.2[1.9]
Current method (No InM)	-18.4 ± 14.9[3.4]	1.33 ± 92.4[1.7]
FSI3	D_x (10^{-3} m)	D_y (10^{-3} m)
Turek and Hron [56]	-2.69 ± 2.53[10.9]	1.48 ± 34.38[5.3]
Kollmannsberger et al. [59]	-2.88 ± 2.71[11.0]	1.48 ± 35.1[5.5]
Current method (InM)	-2.53 ± 2.33[10.6]	1.48 ± 33.1[5.4]
Current method (No InM)	-3.70 ± 3.43[10.0]	1.60 ± 40.7[4.9]

Fig. 18 shows that the vorticity contours of FSI2 when the beam oscillates periodically at four different instants, i.e. $t = 12.12, 12.27, 12.40, 12.54$s, which are marked in Fig. 17. The corresponding velocity magnitude contours of the

beam and the velocity vectors of the surface material points are displayed in Fig. 19. It can be seen that the beam deforms very smoothly.

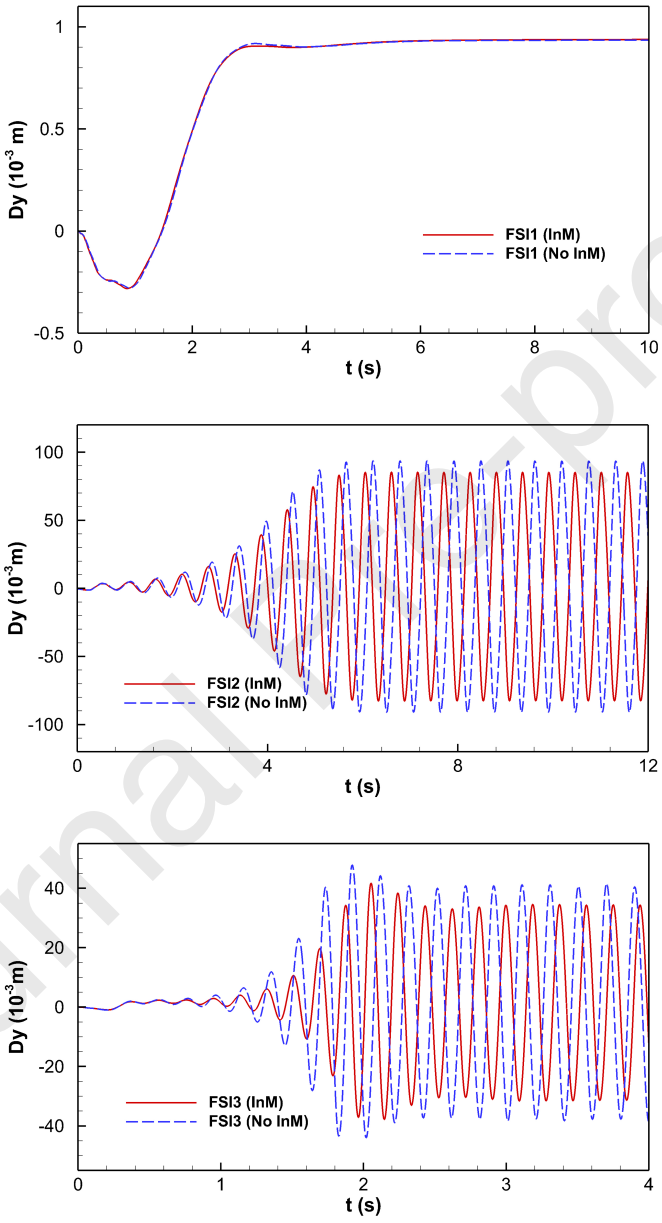

Figure 16: Time history of the vertical displacement of Point A.

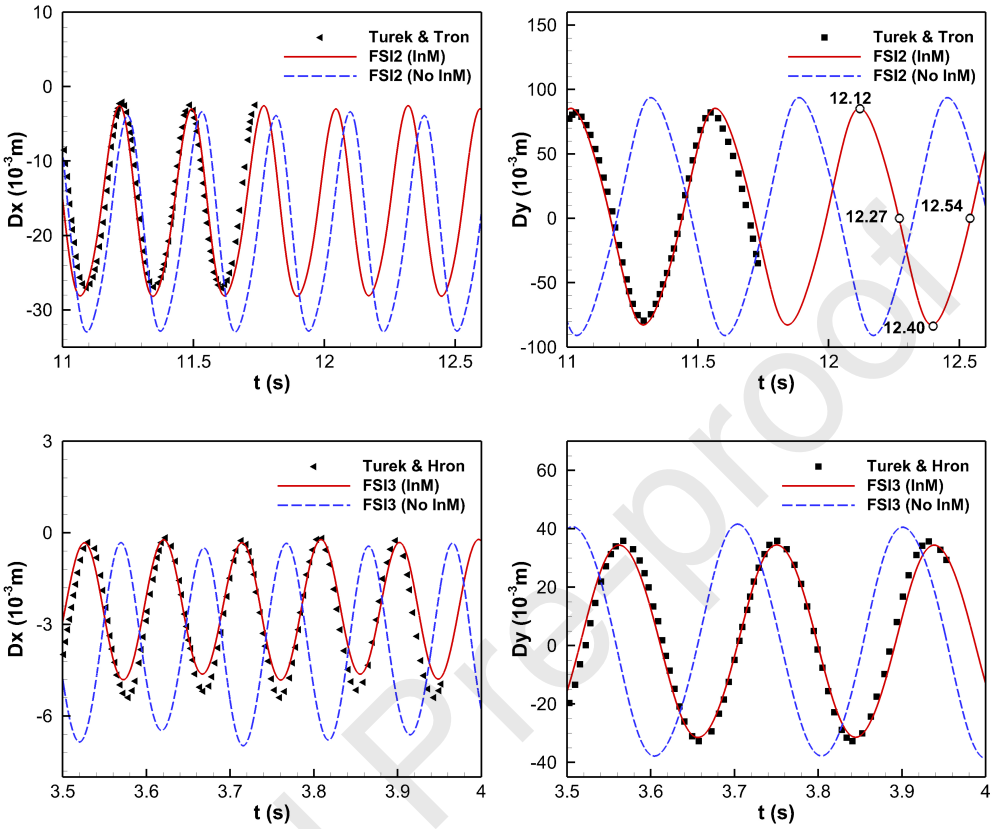

Figure 17: Variation of the displacements D_x and D_y of Point A, comparing with the results of Turek and Hron [56].

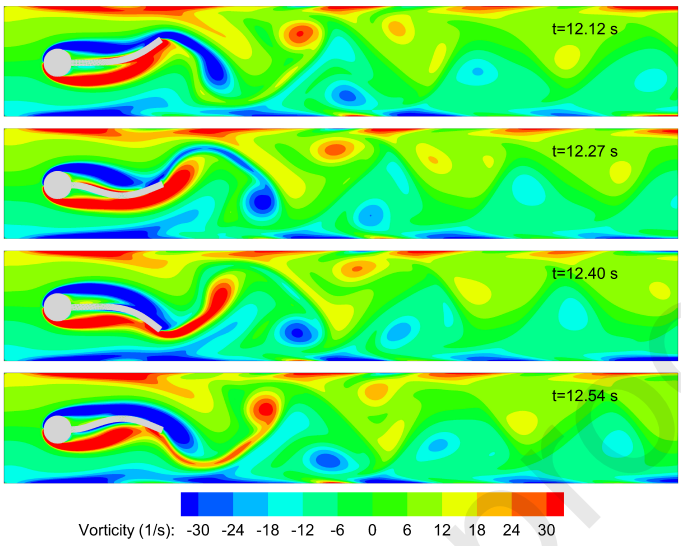

Figure 18: Vorticity contours of the flow field in FSI2 at four different instants.

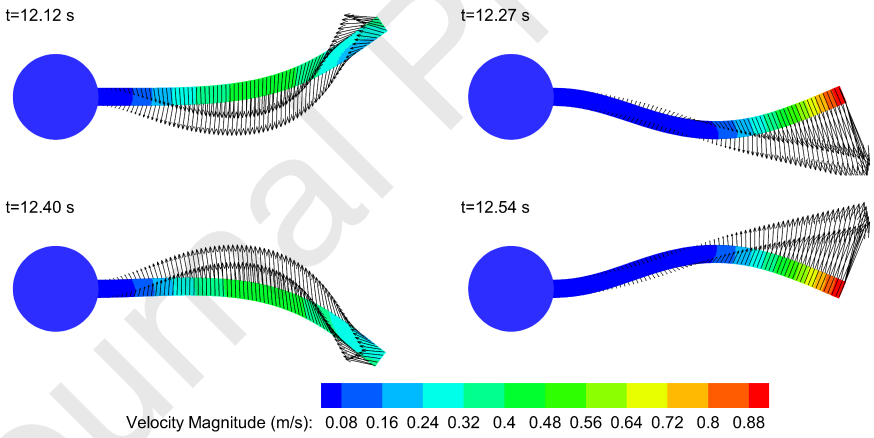

Figure 19: Velocity magnitudes of the beam and velocity vectors of surface material points in FSI2 at four different instants.

To demonstrate the effectiveness of the present approach to capturing the crack and breakup of structures in a flow field, a critical bond stretch $s_c = 0.05$ ($G_c = 7.56$ J/m^2) is assumed in the peridynamic model to allow material

damage. The growth of crack and the movement of the broken beam in the flow field of FSI2 are shown in Fig. 20. At the time of 6.07s, the up left end of the beam is slightly damaged. At the time of 6.82s, a complete breakup at the joint of the beam and the rigid cylinder can be clearly seen. The broken beam is then detached from the rigid cylinder and moves with the fluid towards the outlet. At the time of 7.82s, there is a significant change in the vorticity contour of the flow field, where the size of the vortex attached on the upside of the beam becomes much smaller, and new vortices appear in the gap between the rigid cylinder and the broken beam.

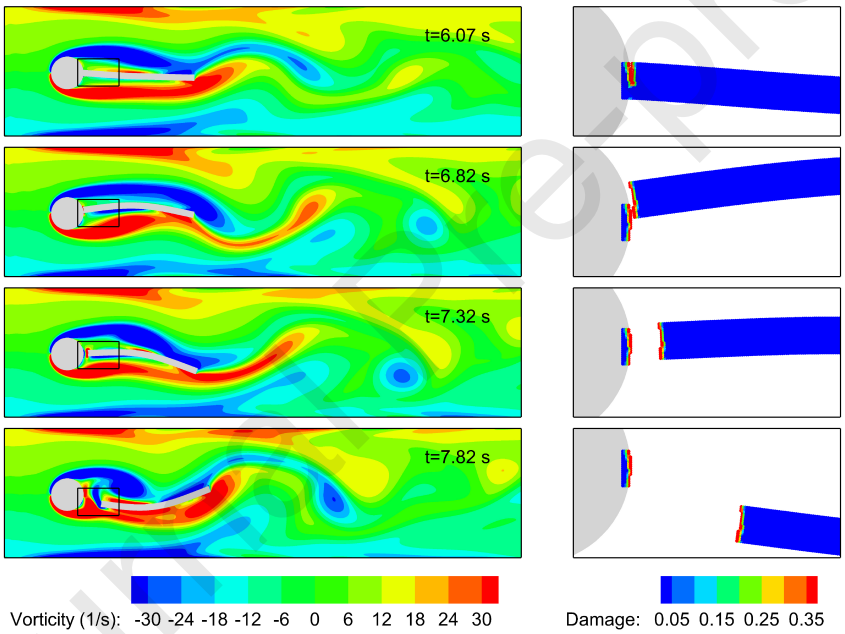

Figure 20: Crack formation and breakup (indicated by the damage of peridynamic material points) of the oscillating beam in FSI2 at the four different instants, and the corresponding vorticity contours of the flow field. Damage here is quantified as the ratio of the number of broken bonds to the total number of bonds for each peridynamic material point.

The current method is implemented with the graphics processing unit (GPU) parallel computation. All the simulations in this work are carried out on a host CPU (Intel(R) Xeon(R) E5-2630 v4 (2.20GHz)) and a single device GPU

(NVIDIA Tesla V100-SXM2-16GB). It can be seen from Table 6 that for the case FSI2, the fluid solver LBM consumes the most time of 7.8 s for a total of 1×10^4 steps, while the computational time for the peridynamic model is almost negligible due to the small number of material points. It should be noted that updating the matrix $\mathbf{A}$ and ω is relatively time-consuming, 2.9 s for 1×10^4 steps, while the total computational time consumed is about 15.1 s. The details of implementing the fluid solver LBM and the relaxed MDF-IBM on a single GPU can be found in Zhang et al. [21, 22, 60], and the GPU implementation of the peridynamic model can refer to the work of Liu and Hong [61].

Table 6: Computational time consumed in FSI2.

Solvers	CLBM	PD	Update $\mathbf{A}$ and ω	IBM ($L_m = 5$)
Number of nodes	$1,027,911$	$7,060$	1017×1017	1017
Time for each solver (s/10^4 steps)	7.8	0.5	2.9	3.1
Time in total (s/10^4 steps)	15.1	CPU: Xeon(R) E5-2630 v4 (2.20GHz) GPU: Tesla V100-SXM2-16GB		

4. Conclusions

A novel strong coupling partition approach for the peridynamic and IB-CLBM models is developed to simulate complex fluid-structure interactions accurately and efficiently. In addition to describing structure deformation, our method can capture crack formation, propagation, breakup of structure. The strong coupling is achieved by adding velocity corrections for the fluid and solid phases simultaneously at each time step, which are calculated by solving a linear system of equations derived from an implicit velocity-correction IB scheme. Therefore, this new strong coupling scheme based on the IBM eliminates the need to iteratively solve the dynamics of the fluid and solid phases at each time step. Moreover, instead of using the time-consuming matrix inversion calculation, the simultaneous velocity corrections are solved with the efficient relaxed MDF scheme of the IBM. Our method is validated rigorously by a range of

cases including the plate with a pre-existing crack under velocity boundary conditions, the sedimentation of an elastic disk, the cross-flow over a flexible beam, and the flow-induced deformation of an elastic beam attached to a rigid cylinder. Moreover, the dynamics of crack formation and breakup of structures in a flow field are inherently captured. Therefore, this novel FSI model exploiting strong coupling of the peridynamic and IB-CLBM models has shown its potential in simulating complex FSI problems involving structural deformation and fracture.

Acknowledgement

This work is supported by the UK Engineering and Physical Sciences Research Council (EPSRC) under grant number EP/P022243/1. The authors would also like to acknowledge the support of JADE GPU Cluster (EPSRC grant number EP/P020275/1) by providing access time through the EPSRC Resource Allocation Panel (Project ID JD034).

Data availability statement

The data that support the findings of this study are available from the corresponding author upon reasonable request.

References

[1] E. S. Di Martino, G. Guadagni, A. Fumero, G. Ballerini, R. Spirito, P. Biglioli, A. Redaelli, Fluid–structure interaction within realistic three-dimensional models of the aneurysmatic aorta as a guidance to assess the risk of rupture of the aneurysm, Medical Engineering & Physics 23 (2001) 647–655.

[2] J. Hong, T. M. Evans, P. L. Mente, Study on the damage mechanism of articular cartilage based on the fluid–solid coupled particle model, Advances in Mechanical Engineering 7 (2015) 1687814015581264.

[3] P. P. Gohil, R. Saini, Coalesced effect of cavitation and silt erosion in hydro turbines—a review, Renewable and Sustainable Energy Reviews 33 (2014) 280–289.

[4] D.-K. Sun, Z. Bo, Numerical simulation of hydrodynamic focusing of particles in straight channel flows with the immersed boundary-lattice Boltzmann method, International Journal of Heat and Mass Transfer 80 (2015) 139–149.

[5] R. M. MacMECCAN, J. R. Clausen, G. P. Neitzel, C. K. Aidun, Simulating deformable particle suspensions using a coupled lattice-boltzmann and finite-element method, Journal of Fluid Mechanics 618 (2009) 13–39.

[6] T. Krüger, F. Varnik, D. Raabe, Efficient and accurate simulations of deformable particles immersed in a fluid using a combined immersed boundary lattice Boltzmann finite element method, Computers & Mathematics with Applications 61 (2011) 3485–3505.

[7] S. Ndanou, N. Favrie, S. Gavrilyuk, Multi-solid and multi-fluid diffuse interface model: Applications to dynamic fracture and fragmentation, Journal of Computational Physics 295 (2015) 523–555.

[8] A. Rahmat, M. Barigou, A. Alexiadis, Deformation and rupture of compound cells under shear: A discrete multiphysics study, Physics of Fluids 31 (2019) 051903.

[9] S. A. Silling, E. Askari, A meshfree method based on the peridynamic model of solid mechanics, Computers and Structures 83 (2005) 1526–1535.

[10] S. A. Silling, M. Epton, O. Weckner, J. Xu, E. Askari, Peridynamic states and constitutive modeling, Journal of Elasticity 88 (2007) 151–184.

[11] E. Madenci, E. Oterkus, Peridynamic Theory and Its Applications, volume 9781461484, Springer New York, New York, NY, 2014.

[12] F. Bobaru, G. Zhang, Why do cracks branch? A peridynamic investigation of dynamic brittle fracture, International Journal of Fracture 196 (2016) 1–40.

[13] S. A. Silling, F. Bobaru, Peridynamic modeling of membranes and fibers, International Journal of Non-Linear Mechanics 40 (2005) 395–409.

[14] C. Sun, Z. Huang, Peridynamic simulation to impacting damage in composite laminate, Composite Structures 138 (2016) 335–341.

[15] E. Madenci, S. Oterkus, Ordinary state-based peridynamics for plastic deformation according to von Mises yield criteria with isotropic hardening, Journal of the Mechanics and Physics of Solids 86 (2016) 192–219.

[16] M. R. Tupek, J. J. Rimoli, R. Radovitzky, An approach for incorporating classical continuum damage models in state-based peridynamics, Computer Methods in Applied Mechanics and Engineering 263 (2013) 20–26.

[17] T. Rabczuk, H. Ren, A peridynamics formulation for quasi-static fracture and contact in rock, Engineering Geology 225 (2016) 0–1.

[18] A. De Rosis, S. Ubertini, F. Ubertini, A partitioned approach for two-dimensional fluid-structure interaction problems by a coupled lattice Boltzmann-finite element method with immersed boundary, Journal of Fluids and Structures 45 (2014) 202–215.

[19] G. Fourey, C. Hermange, D. Le Touzé, G. Oger, An efficient fsi coupling strategy between smoothed particle hydrodynamics and finite element methods, Computer Physics Communications 217 (2017) 66–81.

[20] M. Geier, A. Greiner, J. G. Korvink, Cascaded digital lattice Boltzmann automata for high Reynolds number flow, Physical Review E - Statistical, Nonlinear, and Soft Matter Physics 73 (2006) 1–10.

[21] Y. Zhang, Y. Zhang, G. Pan, S. Haeri, Numerical study of the particle sedimentation in a viscous fluid using a coupled DEM-IB-CLBM approach, Journal of Computational Physics 368 (2018) 1–20.

[22] Y. Zhang, G. Pan, Y. Zhang, S. Haeri, A relaxed multi-direct-forcing immersed boundary-cascaded lattice Boltzmann method accelerated on GPU, Computer Physics Communications (2019) 106980.

[23] E. J. Falagkaris, D. M. Ingram, K. Markakis, I. M. Viola, PROTEUS: A coupled iterative force-correction immersed-boundary cascaded lattice Boltzmann solver for moving and deformable boundary applications, Computers and Mathematics with Applications 75 (2018) 1330–1354.

[24] X. Yu, K. Regenauer-Lieb, F.-B. Tian, A hybrid immersed boundary-lattice boltzmann/finite difference method for coupled dynamics of fluid flow, advection, diffusion and adsorption in fractured and porous media, Computers and Geosciences 128 (2019) 70–78.

[25] J. Ma, Z. Wang, J. Young, J. C. Lai, Y. Sui, F.-B. Tian, An immersed boundary-lattice boltzmann method for fluid-structure interaction problems involving viscoelastic fluids and complex geometries, Journal of Computational Physics 415 (2020) 109487.

[26] D. Lycett-Brown, K. H. Luo, Cascaded lattice Boltzmann method with improved forcing scheme for large-density-ratio multiphase flow at high Reynolds and Weber numbers, Physical Review E 94 (2016) 1–20.

[27] L. Fei, K. H. Luo, C. Lin, Q. Li, Modeling incompressible thermal flows using a central-moments-based lattice Boltzmann method, International Journal of Heat and Mass Transfer 120 (2018) 624–634.

[28] C. S. Peskin, Numerical analysis of blood flow in the heart, Journal of Computational Physics 25 (1977) 220–252.

[29] F. Sotiropoulos, X. Yang, Immersed boundary methods for simulating fluid–structure interaction, Progress in Aerospace Sciences 65 (2014) 1–21.

[30] B. E. Griffith, N. A. Patankar, Immersed methods for fluid–structure interaction, Annual Review of Fluid Mechanics 52 (2020).

[31] F.-B. Tian, H. Luo, L. Zhu, J. C. Liao, X.-Y. Lu, An efficient immersed boundary-lattice boltzmann method for the hydrodynamic interaction of elastic filaments, Journal of Computational Physics 230 (2011) 7266–7283.

[32] W. Wang, Y. Yan, F. Tian, A simple and efficient implicit direct forcing immersed boundary model for simulations of complex flow, Applied Mathematical Modelling 43 (2016) 287–305.

[33] S. Haeri, J. S. Shrimpton, On the application of immersed boundary, fictitious domain and body-conformal mesh methods to many particle multiphase flows, International Journal of Multiphase Flow 40 (2012) 38–55.

[34] S. Haeri, J. S. Shrimpton, A new implicit fictitious domain method for the simulation of flow in complex geometries with heat transfer, Journal of Computational Physics 237 (2013) 21–45.

[35] S. Haeri, J. S. Shrimpton, Fully resolved simulation of particle deposition and heat transfer in a differentially heated cavity, International Journal of Heat and Fluid Flow 50 (2014) 1–15.

[36] W. X. Huang, F. B. Tian, Recent trends and progress in the immersed boundary method, ARCHIVE Proceedings of the Institution of Mechanical Engineers Part C Journal of Mechanical Engineering Science 1989–1996 (vols 203–210) 233 (2019) 095440621984260.

[37] L. Wang, F. B. Tian, J. C. S. Lai, An immersed boundary method for fluid-structure-acoustics interactions involving large deformations and complex geometries, Journal of Fluids and Structures 95 (2020) 102993.

[38] L. Wang, F. B. Tian, Numerical study of flexible flapping wings with an immersed boundary method: Fluid-structure-acoustics interaction, Journal of Fluids and Structures 90 (2019) 396–409.

[39] Y. Zhang, G. Pan, Y. Zhang, S. Haeri, A multi-physics peridynamics-DEM-IB-CLBM framework for the prediction of erosive impact of solid

particles in viscous fluids, Computer Methods in Applied Mechanics and Engineering 352 (2019) 675–690.

[40] F. Dalla Barba, F. Picano, A novel approach for direct numerical simulation of hydraulic fracture problems, Flow, Turbulence and Combustion (2020).

[41] F. Dalla Barba, F. Picano, A new method for fully resolved simulations of fracturing in fluid-structure interaction problems, in: ERCOFTAC Workshop Direct and Large Eddy Simulation, Springer, 2019, pp. 469–475.

[42] Q. Zhang, T. Hisada, Studies of the strong coupling and weak coupling methods in FSI analysis, International Journal for Numerical Methods in Engineering 60 (2004) 2013–2029.

[43] C. Wang, J. D. Eldredge, Strongly coupled dynamics of fluids and rigid-body systems with the immersed boundary projection method, Journal of Computational Physics 295 (2015) 87–113.

[44] U. Lācis, K. Taira, S. Bagheri, A stable fluid–structure-interaction solver for low-density rigid bodies using the immersed boundary projection method, Journal of Computational Physics 305 (2016) 300–318.

[45] A. Goza, T. Colonius, A strongly-coupled immersed-boundary formulation for thin elastic structures, Journal of Computational Physics 336 (2017) 401–411.

[46] S. A. Silling, E. Askari, Peridynamic Modeling of Impact Damage, in: Problems Involving Thermal Hydraulics, Liquid Sloshing, and Extreme Loads on Structures, volume 2004, ASME, 2004, pp. 197–205.

[47] Y. H. Qian, D. D'Humières, P. Lallemand, Lattice BGK Models for Navier-Stokes Equation, EPL (Europhysics Letters) 17 (1992) 479–484.

[48] K. N. Premnath, S. Banerjee, Incorporating forcing terms in cascaded lattice Boltzmann approach by method of central moments, Physical Review E - Statistical, Nonlinear, and Soft Matter Physics 80 (2009).

[49] J. Wu, C. Shu, Implicit velocity correction-based immersed boundary-lattice Boltzmann method and its applications, Journal of Computational Physics 228 (2009) 1963–1979.

[50] K. Suzuki, T. Inamuro, Effect of internal mass in the simulation of a moving body by the immersed boundary method, Computers and Fluids 49 (2011) 173–187.

[51] W. X. Huang, S. J. Shin, H. J. Sung, Simulation of flexible filaments in a uniform flow by the immersed boundary method, Journal of Computational Physics 226 (2007) 2206–2228.

[52] W. X. Huang, H. J. Sung, An immersed boundary method for fluid-flexible structure interaction, Computer Methods in Applied Mechanics and Engineering 198 (2009) 2650–2661.

[53] Z. G. Feng, E. E. Michaelides, Robust treatment of no-slip boundary condition and velocity updating for the lattice-boltzmann simulation of particulate flows, Computers and Fluids 38 (2009) 370–381.

[54] Z. Q. Zhang, G. R. Liu, B. C. Khoo, Immersed smoothed finite element method for two dimensional fluid-structure interaction problems, International Journal for Numerical Methods in Engineering 90 (2012) 1292–1320.

[55] D. Han, G. Liu, S. Abdallah, An Eulerian-Lagrangian-Lagrangian method for solving fluid-structure interaction problems with bulk solids, Journal of Computational Physics 405 (2020) 109164.

[56] S. Turek, J. Hron, Proposal for Numerical Benchmarking of Fluid-Structure Interaction between an Elastic Object and Laminar Incompressible Flow, Springer, Berlin, Heidelberg, Berlin, Heidelberg, 2006.

[57] R. Bhardwaj, R. Mittal, Benchmarking a Coupled Immersed-Boundary-Finite-Element Solver for Large-Scale Flow-Induced Deformation, AIAA Journal 50 (2012) 1638–1642.

[58] Z. Li, J. Favier, A non-staggered coupling of finite element and lattice Boltzmann methods via an immersed boundary scheme for fluid-structure interaction, Computers and Fluids 143 (2017) 90–102.

[59] S. Kollmannsberger, S. Geller, A. Düster, J. Tölke, C. Sorger, M. Krafczyk, E. Rank, Fixed-grid fluid-structure interaction in two dimensions based on a partitioned lattice boltzmann and p-fem approach, International Journal for Numerical Methods in Engineering 79 (2010) 817–845.

[60] Y. Zhang, G. Pan, Q. Huang, Iccm2016: The implementation of two-dimensional multi-block lattice boltzmann method on gpu, International Journal of Computational Methods (2017) 1840002.

[61] W. Liu, J. W. Hong, Discretized peridynamics for brittle and ductile solids, International Journal for Numerical Methods in Engineering 89 (2012) 1028–1046.